

Paleoceanography and Paleoclimatology®

RESEARCH ARTICLE

10.1029/2023PA004629

Key Points:

- Brazil Margin $\delta^{13}\text{C}$ and $[\text{CO}_3^{2-}]$ records suggest the Atlantic Meridional Overturning Circulation weakened during each deglaciation of the last 150,000 years
- Movement of northern source water yields larger $\delta^{13}\text{C}$ and $[\text{CO}_3^{2-}]$ anomalies at 1,800 m during MIS 2, 4, and 6 and at 2,300 m during MIS 5
- The dynamic nature of Atlantic watermass structure complicates the diagnosis of overturning patterns on glacial-interglacial timescales

Correspondence to:

M. Garity,
monica.garity@uconn.edu

Citation:

Garity, M., & Lund, D. (2024). Multi-proxy evidence for Atlantic Meridional Overturning Circulation (AMOC) weakening during deglaciations of the past 150,000 years. *Paleoceanography and Paleoclimatology*, 39, e2023PA004629. <https://doi.org/10.1029/2023PA004629>

Received 13 MAR 2023

Accepted 20 NOV 2023

Multi-Proxy Evidence for Atlantic Meridional Overturning Circulation (AMOC) Weakening During Deglaciations of the Past 150,000 Years

Monica Garity¹  and David Lund¹ 

¹Department of Marine Sciences, University of Connecticut, Groton, CT, USA

Abstract Despite decades of research, the cause of deglaciations is not fully understood, leaving a critical gap in our understanding of Earth's climate system. During the most recent deglaciation (Termination I (T I)), abrupt declines in the stable carbon isotope ratio ($\delta^{13}\text{C}$) of benthic foraminifera occurred throughout the mid-depth (1,500–2,500 m) Atlantic. The spatial pattern in $\delta^{13}\text{C}$ anomalies was likely due to Atlantic Meridional Overturning Circulation (AMOC) weakening and the accumulation of respired carbon, which also yields negative excursions in carbonate ion concentration ($[\text{CO}_3^{2-}]$). To investigate whether a similar pattern occurred during prior deglaciations, we developed $\delta^{13}\text{C}$ and $[\text{CO}_3^{2-}]$ records from 1,800 and 2,300 m water depth in the Southwest Atlantic spanning the last 150 ka. The new records reveal negative $\delta^{13}\text{C}$ and $[\text{CO}_3^{2-}]$ anomalies during Termination II (TII) and the smaller deglaciations of Marine Isotope Stages (MIS) 4/3, 5b/a, and 5d/c, suggesting AMOC weakening is a common feature of deglaciation. The anomalies are more pronounced in the shallower core following MIS 2, 4, and 6 and in the deeper core following MIS 5b and 5d. The depth-dependent pattern is most likely due to shoaling of Northern Source Water during glacial maxima and deepening during interglacial intervals. Comparison of $[\text{CO}_3^{2-}]$ records from TI and TII suggests similar levels of carbon accumulation in the mid-depth Atlantic. The Brazil Margin $\delta^{13}\text{C}$ and $[\text{CO}_3^{2-}]$ results indicate the AMOC plays a key role in the series of events causing deglaciation, regardless of differences in orbital configuration, ice volume, and mean global temperature.

1. Introduction

Earth's climate during the late Pleistocene is characterized by the advance and retreat of large continental ice sheets on ~100,000-year timescales. While it has long been known that changes in insolation pace glacial-interglacial cycles (Hays et al., 1976; Imbrie et al., 1992, 1993), internal climate system mechanisms are required to explain the full magnitude of glacial-interglacial cycle variability (Cheng et al., 2009; Shakun et al., 2012; Sigman & Boyle, 2000). Abrupt increases in global mean sea level, temperature, and atmospheric pCO_2 during deglaciations are particularly difficult to explain given low frequency changes in insolation. The most recent deglaciation, or Termination I (TI; 10–18 kyr BP), was marked by a 120–130 m rise in global sea level (Clark et al., 2009), a 6–7°C warming of global mean surface temperature (Osman et al., 2021; Tierney et al., 2020), and an 80 ppmv increase in atmospheric CO_2 (Marcott et al., 2014) (Figure 1). Models forced with insolation alone yield relatively modest changes in Earth's climate, indicating internal mechanistic feedbacks are required to explain deglaciations (Shakun et al., 2012). An improved understanding of the mechanisms that drive deglaciation can be achieved by reconstructing and comparing key climate system parameters across multiple glacial-interglacial transitions.

The Atlantic Meridional Overturning Circulation (AMOC) likely plays a central role in triggering deglaciations. In the North Atlantic region, TI began with Heinrich Stadial 1 (HS1; 17.5–14.5 kyr BP), followed by abrupt warming into the Bølling Allerød (BA; 14.7–12.7 kyr BP), a return to glacial-like conditions during the Younger Dryas (YD; 12.8–11.7 kyr BP), and subsequent warming into the Holocene (Cheng et al., 2020; Lourdantou et al., 2010; Monnin et al., 2001; Rasmussen et al., 2006). The TI pattern is due to AMOC weakening during HS1, strengthening during the BA, and weakening once again during the YD (Chen et al., 2015; McManus et al., 2004). Simulated collapse of the AMOC increases the residence time of mid-depth waters, leading to the accumulation of isotopically light respired carbon, which yields $\delta^{13}\text{C}$ anomalies in the North and South Atlantic (Gu et al., 2021; Schmittner & Lund, 2015). Consistent with model results, widespread negative $\delta^{13}\text{C}$ anomalies occurred in the mid-depth (1,500–2,500 m) Atlantic during HS1, with the largest signals observed in the North Atlantic and progressively smaller anomalies to the south (McManus et al., 1999; Oppo et al., 2015; Praetorius

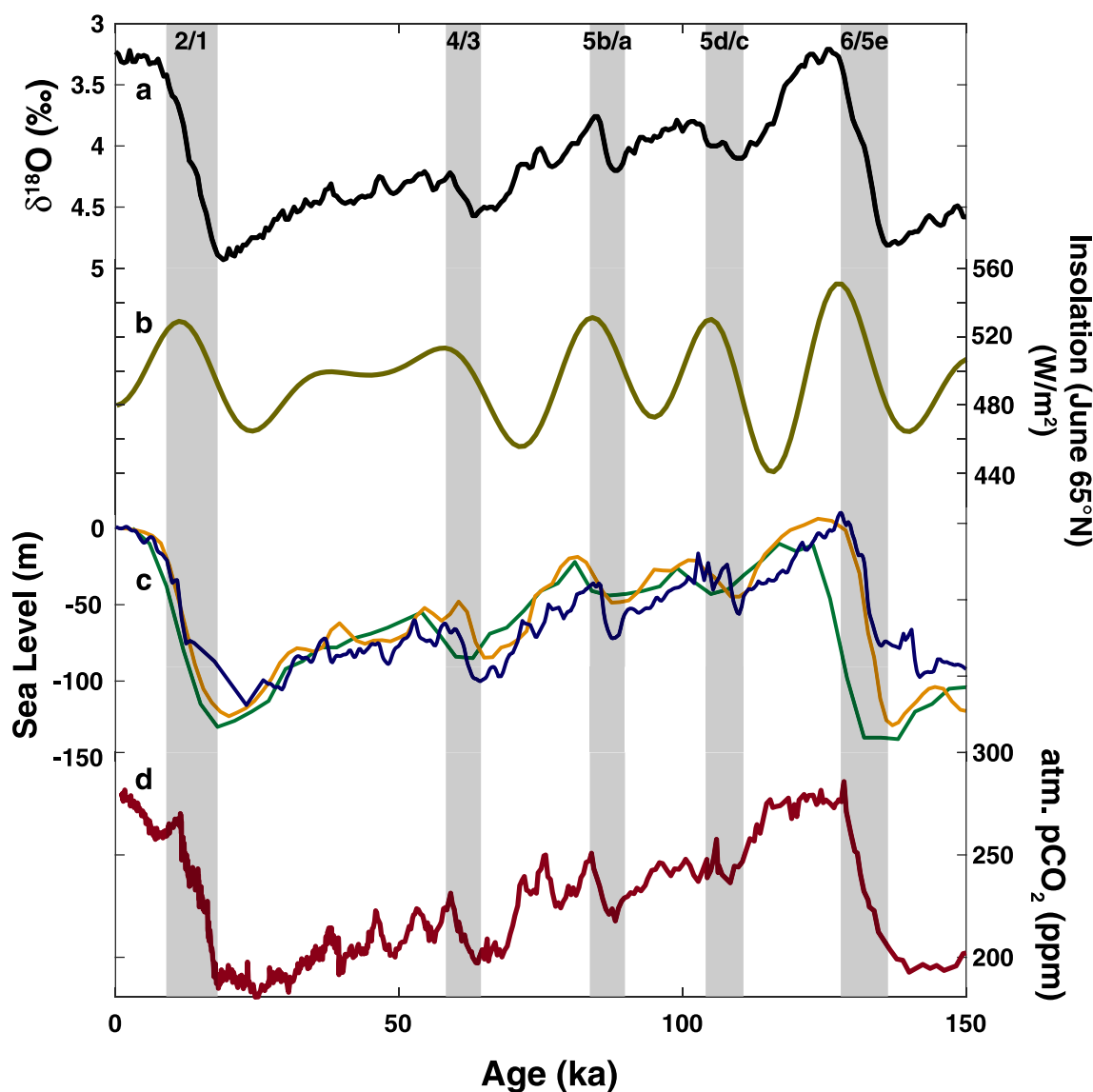


Figure 1. Key climate parameters for the past 150 ka. (a) Global benthic $\delta^{18}\text{O}$ stack (Lisiecki & Stern, 2016), reflecting changes in ice volume and mean deep ocean temperature. (b) Insolation, June 21 at 65°N (Laskar et al., 2004; Tzedakis et al., 2017). (c) Sea level records from three independent age models and methods. Purple curve is based on Red Sea planktonic $\delta^{18}\text{O}$ (Grant et al., 2012; Rohling et al., 2009), green curve is from a global stack of planktonic $\delta^{18}\text{O}$ and SST records, where the age model is based on LR04 (Shakun et al., 2015), orange curve is based on benthic $\delta^{18}\text{O}$ and a SPECMAP-derived age model corrected using coral U-Th dates during Termination II (Waelbroeck et al., 2002). (d) Composite atmospheric $p\text{CO}_2$ record from Bereiter et al. (2015), with records from Rubino et al. (2013), MacFarling Meure et al. (2006), Monnin et al. (2001, 2004), Marcott et al. (2014), Ahn and Brook (2014), Bereiter et al. (2012), and Schneider et al. (2013). Deglaciations are identified by gray vertical bars with MIS labels at top.

et al., 2008; Rickaby & Elderfield, 2005; Tessin & Lund, 2013). Reconstructions of B/Ca, a proxy for seawater carbonate ion concentration ($[\text{CO}_3^{2-}]$), are consistent with accumulation of respired carbon during HS1, with larger negative $[\text{CO}_3^{2-}]$ anomalies occurring in the North Atlantic than in the South Atlantic (Lacerra et al., 2017; Yu et al., 2010). Together, $[\text{CO}_3^{2-}]$ and $\delta^{13}\text{C}$ can be used to assess AMOC variability and its role in deglaciations.

AMOC weakening also occurred during Termination II (TII) (125–135 ka), but with a different structure. Unlike TI, $^{231}\text{Pa}/^{230}\text{Th}$ and $\delta^{13}\text{C}$ records suggest AMOC was weak throughout much of TII and did not recover until the following interglacial interval (Böhm et al., 2015; Deaney et al., 2017; Oppo et al., 1997; Venz et al., 1999). Several mechanisms have been proposed to explain the lack of a BA-like event during TII. Higher boreal summer-time insolation and greater ice melt may have suppressed the AMOC throughout TII (Carlson, 2008; Deaney et al., 2017; Obase et al., 2021). Or the lack of AMOC recovery may be the result of a positive feedback, where

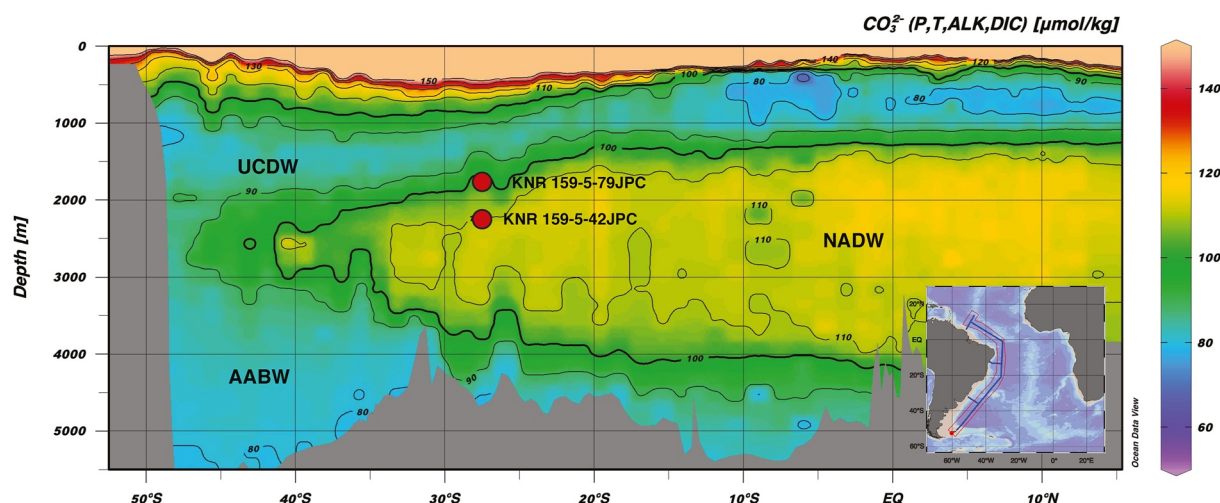


Figure 2. Locations of the cores used in this study (red circles) overlain on the World Ocean Circulation Experiment A17 $[\text{CO}_3^{2-}]$ section (Schlitzer, 2015). Major watermasses include high $[\text{CO}_3^{2-}]$ North Atlantic Deep Water and low $[\text{CO}_3^{2-}]$ Upper Circumpolar Deep Water and Antarctic Bottom Water (AABW). Contour intervals are 10 $\mu\text{mol/kg}$. Location of the A17 section is shown on inset map.

a weaker AMOC causes sub-surface warming, which in turn accelerates ice sheet melt and freshwater forcing (Clark et al., 2020; Marcott et al., 2011). A larger Eurasian ice sheet during TII with low elevation mass susceptible to oceanic forcing may have also supplied more meltwater to the North Atlantic, suppressing the AMOC (Clark et al., 2020). Consistent with this idea, sea level rose more quickly during TII than TI and it was higher during the last interglacial period (Clark et al., 2020; Dyer et al., 2021) (Figure 1). Thus, AMOC weakening appears to play a central role in the timing and structure of the last two glacial terminations.

The deglaciations during Marine Isotope Stage (MIS) transitions 4/3, 5b/a, and 5d/c provide further opportunities to investigate the link between ice sheet retreat and the ocean circulation. Compared to Terminations I and II, the three smaller deglaciations were characterized by relatively modest changes in $\delta^{18}\text{O}$, sea level, and atmospheric pCO_2 (Figure 1). They also occurred when atmospheric pCO_2 and global ice volume were at intermediate levels, while TI and TII began when pCO_2 and sea level were at their lowest values of the last 150 ka. Taken together, the five most recent deglaciations occurred under a range of climate boundary conditions; the only common factor between them is increasing boreal summertime insolation (Hays et al., 1976; Imbrie et al., 1992) (Figure 1). It has been hypothesized that northern hemisphere warming and ice melt caused freshening of the North Atlantic and subsequent weakening of the AMOC, which may have in turn promoted further deglaciation through subsurface oceanic warming and ice shelf collapse (Clark et al., 2020). A key prediction of this hypothesis is that AMOC weakening should be common feature of all deglaciations. Here we evaluate AMOC variability using new benthic $\delta^{13}\text{C}$ and B/Ca records from the mid-depth Brazil Margin spanning the time interval from 50 to 150 ka. Given that $\delta^{13}\text{C}$ and B/Ca are qualitative tracers of AMOC variability, we are unable to quantify changes in AMOC strength during deglaciations. However, prior work at the Brazil Margin has shown that negative anomalies in $\delta^{13}\text{C}$ and $[\text{CO}_3^{2-}]$ during HS1 are due to accumulation of respired carbon in the mid-depth Atlantic, consistent with the simulated pattern due to AMOC weakening (Gu et al., 2021; Hertzberg et al., 2016; Lacerra et al., 2017, 2019; Schmittner & Lund, 2015). When used in conjunction with kinematic proxies such as $^{231}\text{Pa}/^{230}\text{Th}$, $\delta^{13}\text{C}$ and $[\text{CO}_3^{2-}]$ can be used to infer intervals of AMOC weakening and associated changes in carbon cycling.

The cores used in this study are KNR159-5-79JPC (1,830 m, 27.49°S, 46.33°W) and KNR159-5-42JPC (2,296 m, 27.76°S, 46.03°W). Today the deeper core site is bathed primarily in North Atlantic Deep Water (NADW) while the shallower site is bathed in a combination of NADW and Upper Circumpolar Deep Water (Figure 2). For the remainder of the paper, we refer to deep water originating from the North Atlantic as Northern Source Water (NSW), rather than NADW or Glacial North Atlantic Intermediate Water, the latter being specific to the Last Glacial Maximum (LGM) interval. Vertical profiles of $\delta^{13}\text{C}$ from the Brazil Margin indicate the core of NSW was located near 2,500 m during the Holocene, while during the LGM it was located near 1,800 m (Curry & Oppo, 2005; Lund et al., 2015). Therefore, the two cores are ideally suited to track changes in NSW properties across glacial-interglacial periods. Mid-depth $[\text{CO}_3^{2-}]$ and $\delta^{13}\text{C}$ records from the Southwest Atlantic have already

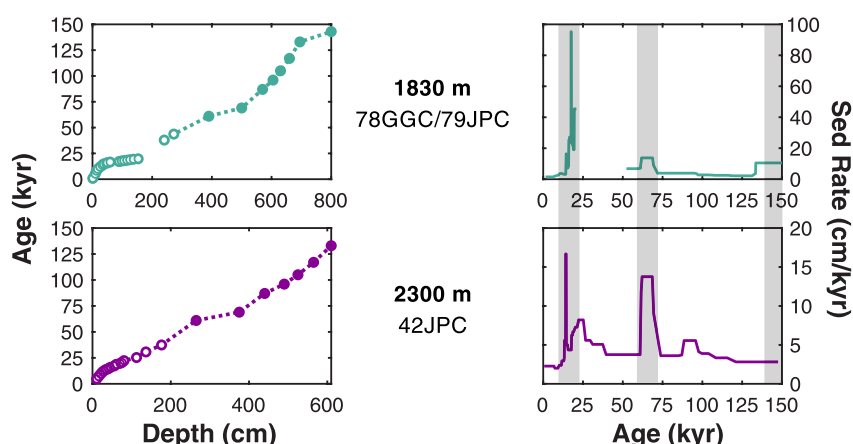


Figure 3. Age models and sedimentation rates for KNR159-5-79JPC/KNR159-5-78GGC and KNR159-5-42JPC from 0 to 150 ka (Shub et al., 2024). Left: Age models are based on oxygen isotope stratigraphy (closed symbols) and radiocarbon-based calendar ages (open symbols). Right: Implied sedimentation rates based on each age model. Vertical gray bars denote glacial marine isotope stages. Note that sedimentation rates tend to be higher during glacial intervals.

been generated for the last deglaciation (Lacerra et al., 2017; Tessin & Lund, 2013), so the records presented here allow for direct comparison of the last two terminations and smaller deglaciations of the last 150 kyr.

2. Methods

2.1. Core Sampling and Stable Isotopes

Samples were taken at varying depths in cores 79JPC and 42JPC to achieve an average temporal resolution of 2–3 kyr. Sediment samples were freeze dried, washed over a 63 μm sieve and dried at 40°C. Each sample was picked for the benthic foraminifer *Cibicidoides wuellerstorfi* (>250 μm size fraction) using a binocular microscope. The specimens were analyzed for $\delta^{18}\text{O}$ and $\delta^{13}\text{C}$ using standard procedures (Ostermann & Curry, 2000). Samples were run on a Thermo MAT 253 triple collector stable isotope ratio mass spectrometer coupled to a Kiel IV carbonate preparation device at the Stable Isotope Laboratory at the University of Michigan. Data were converted to Vienna Pee Dee Belemnite (VPDB) using NBS 19 ($n = 48$, $\delta^{13}\text{C} = 1.96 \pm 0.04$, $\delta^{18}\text{O} = -2.18 \pm 0.08\text{‰}$) and NBS 18 ($n = 13$, $\delta^{13}\text{C} = -5.01 \pm 0.05$, $\delta^{18}\text{O} = -22.97 \pm 0.09\text{‰}$). The Atlantis II standard ($n = 26$, $\delta^{13}\text{C} = 0.91 \pm 0.06$, $\delta^{18}\text{O} = 3.45 \pm 0.06\text{‰}$) was also used to monitor the heavier $\delta^{18}\text{O}$ values associated with this study. All stable isotope analyses were performed on individual shells to facilitate identification of samples affected by bioturbation.

2.2. Age Models

The age models for cores 79JPC and 42JPC are based on oxygen isotope stratigraphy. Benthic $\delta^{18}\text{O}$ records were aligned with the Lisiecki and Stern (2016) (LS16) $\delta^{18}\text{O}$ stack for the deep South Atlantic (2,000–5,000 m; 70°S–0; 70°W–30°E). Compared to LR04 (Lisiecki & Raymo, 2005), the LS16 stack improves on age control during TII, MIS 5, and MIS 4 by using more recent sea level reconstructions (Lisiecki & Stern, 2016). Records were aligned with LS16 by matching the relative amplitudes of the $\delta^{18}\text{O}$ peaks and tie points were chosen at intervals where the rate of $\delta^{18}\text{O}$ change is greatest. The number of age model tie points were minimized to avoid over-tuning; for cores 79JPC and 42JPC, we used eight tie points for the 50–150 kyr interval (Figure 3). Simple linear interpolation was used to determine ages for samples between each tie point. Sedimentation rates in the sampled sections range from ~2 to 15 cm/kyr for both cores (Figure 3). Sedimentation rates are higher during glacial periods (e.g., MIS 4 and 6) and lower during interglacial intervals (e.g., MIS 5). The pattern is consistent with the sedimentation rate differences between the LGM and Holocene in other Brazil Margin cores (Shub et al., 2024).

2.3. B/Ca Analysis

An average of 5 *C. wuellerstorfi* tests were used for each B/Ca analysis. Following the procedure outlined in Yu and Elderfield (2007), samples were crushed between two slides under a microscope to confirm each chamber

Table 1
Hydrographic Parameters Used to Estimate Modern $[\text{CO}_3^{2-}]$ at the Two Core Sites

Core	Water depth (m)	Potential temp ($^{\circ}\text{C}$)	Salinity	$[\text{PO}_4^{3-}]$ ($\mu\text{mol/kg}$)	$[\text{SiO}_3^{2-}]$ ($\mu\text{mol/kg}$)	Avg. ALK ($\mu\text{mol/kg}$)	Avg. ΣCO_2 ($\mu\text{mol/kg}$)	$[\text{CO}_3^{2-}]$ ($\mu\text{mol/kg}$)
79JPC	1,830	3.81	34.90	1.7	30	2,310	2,185	93.4
42JPC	2,296	2.91	34.94	1.5	35	2,313	2,175	99.3

was ruptured to facilitate more complete cleaning. All subsequent steps were performed in a laminar flow hood to minimize sample contamination. Crushed samples were washed into 600 μL centrifuge tubes with Milli-Q water and sonicated for 45 s to bring clays into suspension. The resulting supernatant was then siphoned out and the procedure was repeated 1–2 times depending on the amount of clay present. The same procedure was repeated twice with methanol until the supernatant was clear after sonication. After the methanol rinsing steps, the sample was rinsed one final time with Milli-Q water. Samples were then viewed under a microscope to identify and remove any foreign materials with a dual-haired brush. The samples were oxidatively cleaned to remove organic matter using a buffered H_2O_2 solution (100 μL 30% v/v H_2O_2 + 10 ml 0.1 M NaOH). Reductive cleaning was not performed as this cleaning step was shown to be unnecessary in B/Ca analysis (Yu & Elderfield, 2007). Samples were then leached using a weak acid solution of 0.001 M HNO_3 .

After the cleaning procedure was complete, samples were dissolved in 500 μL of 2% HNO_3 before being analyzed for B/Ca on an Element-2 ICP-MS and ESI SC-2DX autosampler in the UConn Avery Point Paleoclimate Laboratory. Each sample was matrix matched to the calcium concentration of the standard used in the final analysis to avoid any matrix effects resulting for sample-standard mismatches. Lacerra et al. (2019) showed that matrix effects have a minimal influence on B/Ca analyses in the range of calcium concentrations relevant for this study. Nonetheless, the majority of samples were matrix matched to 100 ppm standards, typically within 10 ppm. Occasionally, smaller samples were separately matched to standards at 50–60 ppm to minimize any matrix effects.

2.4. Conversion to $[\text{CO}_3^{2-}]$ and ΣCO_2 From B/Ca

In order to convert down-core variations in B/Ca to $[\text{CO}_3^{2-}]$, it is first necessary to calculate the modern $[\text{CO}_3^{2-}]$ for each core site. Modern carbonate ion values were estimated using the potential temperature, salinity, $[\text{PO}_4^{3-}]$, $[\text{SiO}_3^{2-}]$, average alkalinity, and average ΣCO_2 data listed in Table 1. Hydrographic parameters for 79JPC are based on those for the companion gravity core 78GGC (Lacerra et al., 2017). For 42JPC, potential temperature and salinity were estimated using CTD data from cruise KNR159-5 while $[\text{PO}_4^{3-}]$ and $[\text{SiO}_3^{2-}]$ were estimated from World Ocean Circulation Experiment (WOCE) Atlas Volume 3, section A10 which intersects the Brazil Margin at 28°S (Koltermann et al., 2011, http://sam.ucsd.edu/whp_atlas/atlantic/a10/sections/sct_menu.htm). Average alkalinity and average ΣCO_2 were estimated using data from the WOCE station at 43.58°W and 28.83°S . We used only alkalinity and ΣCO_2 values where potential densities were within 0.05 kg/m^3 of the core site to account for sloping isopycnals at the Brazil Margin, similar to Lacerra et al. (2017). $[\text{CO}_3^{2-}]$ for the 42JPC and 79JPC sites was estimated using the hydrographic parameters in Table 1 and $\text{CO}_2\text{sys_v2.1}$ (Pierrot et al., 2006, <https://cdiac.ess-dive.lbl.gov/ftp/co2sys/>).

B/Ca is a proxy for the degree of carbonate ion saturation, making it necessary to estimate the modern saturated carbonate ion concentration defined as: $[\text{CO}_3^{2-}]_{\text{sat}} = [\text{CO}_3^{2-}]/\Omega_{\text{calcite}}$, where Ω_{calcite} is calculated using $\text{CO}_2\text{sys_v2.1}$. Downcore estimates of $[\text{CO}_3^{2-}]$ were determined using the global core top calibration for *C. wuellerstorfi*: $\text{B/Ca} = 1.14 \times ([\text{CO}_3^{2-}] - [\text{CO}_3^{2-}]_{\text{sat}}) + 177$ (Yu & Elderfield, 2007), which has a calibration uncertainty of $\pm 5 \mu\text{mol/kg}$ (Yu & Elderfield, 2007). ΣCO_2 can then be estimated using the empirical relationship: $\Sigma\text{CO}_2 \approx \text{ALK} - [\text{CO}_3^{2-}]/0.6$ (Yu et al., 2016). Given that $[\text{CO}_3^{2-}]$ is affected by alkalinity and ΣCO_2 , both parameters need to be considered when interpreting down-core reconstructions of $[\text{CO}_3^{2-}]$.

3. Results

3.1. Stable Isotopes

Benthic $\delta^{18}\text{O}$ results for both the shallower core (1,800 m) and deeper core (2,300 m) outline the expected glacial-interglacial pattern for 50–150 ka (Figure 4). In each core, TII is identified by an abrupt decrease in $\delta^{18}\text{O}$

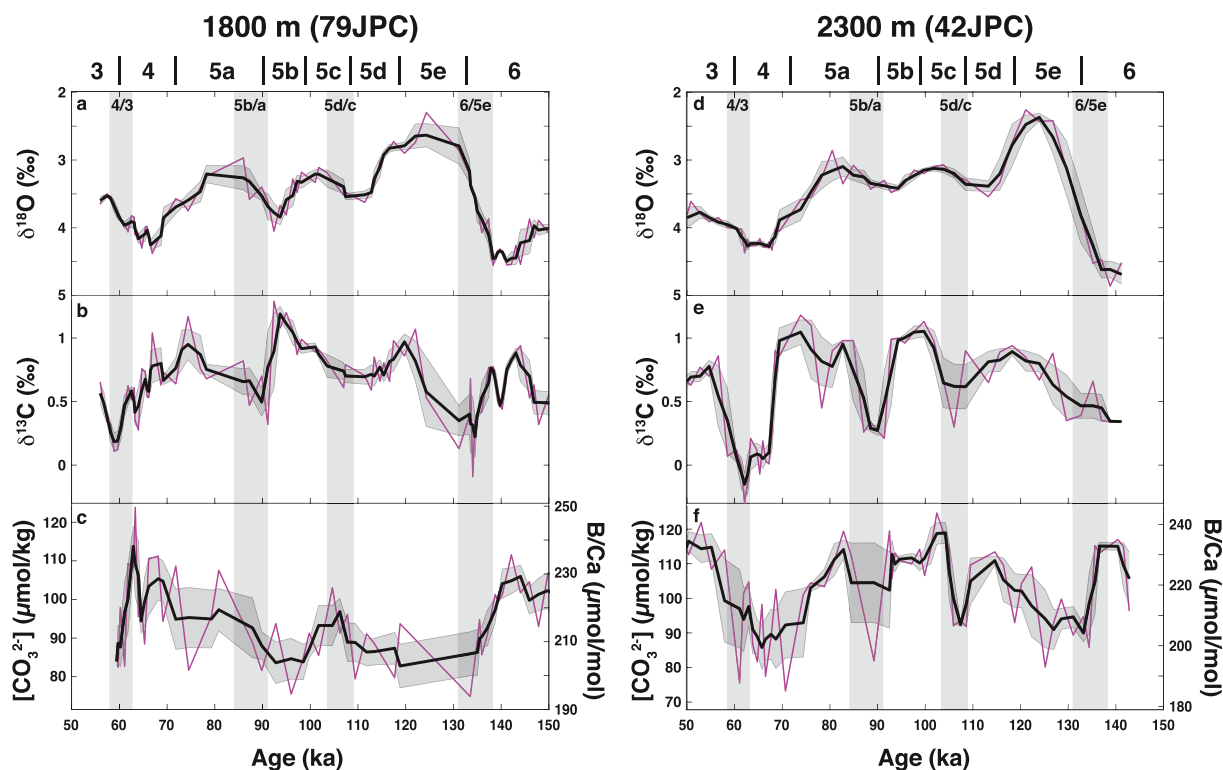


Figure 4. Benthic foraminiferal $\delta^{18}\text{O}$, $\delta^{13}\text{C}$, and $[\text{CO}_3^{2-}]$ results from 50 to 150 ka. (a, d) $\delta^{18}\text{O}$ times series for 1,800 m and 2,300 m water depth, respectively. (b, e) $\delta^{13}\text{C}$ times series. (c, f) B/Ca (right axis) and derived $[\text{CO}_3^{2-}]$ (left axis). In each panel, the black line is a 3-point running average, the purple line represents the average at each stratigraphic level, and the gray envelope is the standard error on the running mean. Vertical gray bars denote each deglaciation, with MIS labels on top x-axes.

starting at ~ 138 ka, which reflects the combined influence of a ~ 120 m rise in sea level (Grant et al., 2012; Shakun et al., 2015; Waelbroeck et al., 2002) and deep sea temperature increase of $\sim 3^\circ\text{C}$ (Cutler et al., 2003). By comparison, sea level rose by only ~ 25 – 45 m during the smaller deglaciations of MIS 5d/c and 5b/a (Grant et al., 2012; Shakun et al., 2015; Waelbroeck et al., 2002) and deep-sea temperatures rose by $\sim 1^\circ\text{C}$ (Cutler et al., 2003). The long-term trend of increasing $\delta^{18}\text{O}$ after TII represents the buildup of continental ice sheets and decreasing deep-sea temperature leading into the LGM.

The Brazil Margin benthic $\delta^{13}\text{C}$ results are characterized less by long-term trends and more by abrupt negative anomalies on deglaciations. During TII, $\delta^{13}\text{C}$ decreased by $0.46 \pm 0.14\text{‰}$ at 1,800 m (Figure 4), where the anomaly is calculated by differencing mean values for MIS 6 and the interval of deglaciation (Table 2). The lack of a $\delta^{13}\text{C}$ anomaly at 2,300 m is likely because the core of NSW was shallower during the preceding glacial interval (i.e., MIS 6). At 1,800 m, $\delta^{13}\text{C}$ nearly recovers to MIS 6 values by the end of MIS 5e. At 2,300 m, $\delta^{13}\text{C}$ is higher at the end of MIS 5e than MIS 6, likely due to deepening of ^{13}C -enriched NSW during TII. At the MIS 5d/c deglaciation, there is a negative $\delta^{13}\text{C}$ anomaly at 2,300 m but not at 1,800 m. At 1,800 m, $\delta^{13}\text{C}$ decreased from MIS 5e to 5d, then increased during MIS 5c and b, reaching a maximum value at ~ 93 ka. During the MIS 5b/a deglaciation, $\delta^{13}\text{C}$ decreased by $0.76 \pm 0.03\text{‰}$ at 2,300 m and then recovered to MIS 5b levels by ~ 80 ka. Benthic $\delta^{13}\text{C}$ also decreased by $0.54 \pm 0.12\text{‰}$ at 1,800 m, but the values did not immediately recover to pre-deglacial values, unlike the pattern at 2,300 m. Finally, during the MIS 4/3 transition, there is a small ($\sim 0.2\text{‰}$) decrease in $\delta^{13}\text{C}$ at 2,300 m, superimposed on the very low $\delta^{13}\text{C}$ background values during MIS 4. At 1,800 m, $\delta^{13}\text{C}$ gradually decreased during MIS 4 and then showed an abrupt negative anomaly of $\sim 0.4\text{‰}$ at the MIS 4/3 transition. The largest negative shift in $\delta^{13}\text{C}$ in either record occurred at the beginning of MIS 4 at 2,300 m ($-0.95 \pm 0.10\text{‰}$). In contrast, $\delta^{13}\text{C}$ at 1,800 m showed little change, highlighting the large vertical gradient in $\delta^{13}\text{C}$ at ~ 2 km water depth during MIS 4.

3.2. $[\text{CO}_3^{2-}]$

Unlike the $\delta^{13}\text{C}$ records, the $[\text{CO}_3^{2-}]$ results reveal negative anomalies at both water depths during TII. At 2,300 m, $[\text{CO}_3^{2-}]$ decreased by $23 \pm 3 \mu\text{mol/kg}$ (Figure 4). The TII signal at 1,800 m is more difficult to estimate. Due to

Table 2
Time Intervals Used to Calculate $\delta^{13}\text{C}$ and $[\text{CO}_3^{2-}]$ Anomalies For Each Deglaciation, Where There is More Than One Data Point Before and During the Deglaciation

	MIS 6/5e 1,800 m	MIS 6/5e 2,300 m	MIS 5d/c 1,800 m	MIS 5d/c 2,300 m	MIS 5b/a 1,800 m	MIS 5b/a 2,300 m	MIS 4/3 1,800 m	MIS 4/3 2,300 m
$\delta^{13}\text{C}$	$\delta^{13}\text{C}$	$\delta^{13}\text{C}$	$\delta^{13}\text{C}$	$\delta^{13}\text{C}$	$\delta^{13}\text{C}$	$\delta^{13}\text{C}$	$\delta^{13}\text{C}$	$\delta^{13}\text{C}$
Time Interval (glacial)	137–138 ka $n = 6$	137–141 ka $n = 4$	111–113 ka $n = 5$	–	94–98 ka $n = 5$	93–100 ka $n = 5$	63–69 ka $n = 13$	63–68 ka $n = 7$
Time Interval (deglacial)	131–134 ka $n = 5$	129–132 ka $n = 3$	103–107 ka $n = 5$	–	87–91 ka $n = 3$	87–91 ka $n = 4$	58–61 ka $n = 6$	58–62 ka $n = 5$
Anomaly	$-0.46 \pm 0.14\text{‰}$	$0.03 \pm 0.08\text{‰}$	$0.026 \pm 0.08\text{‰}$	–	$-0.54 \pm 0.12\text{‰}$	$-0.76 \pm 0.03\text{‰}$	$-0.36 \pm 0.11\text{‰}$	$-0.16 \pm 0.09\text{‰}$
$[\text{CO}_3^{2-}]$	$[\text{CO}_3^{2-}]$	$[\text{CO}_3^{2-}]$	$[\text{CO}_3^{2-}]$	$[\text{CO}_3^{2-}]$	$[\text{CO}_3^{2-}]$	$[\text{CO}_3^{2-}]$	$[\text{CO}_3^{2-}]$	$[\text{CO}_3^{2-}]$
Time Interval (glacial)	139–142 ka $n = 3$	137–139 ka $n = 2$	111–113 ka $n = 3$	111–113 ka $n = 3$	109–116 ka $n = 3$	–	63–69 ka $n = 7$	–
Time Interval (deglacial)	133 ka $n = 1$	128–135 ka $n = 5$	104–107 ka $n = 3$	104–107 ka $n = 3$	105–109 ka $n = 3$	–	59–61 ka $n = 4$	–
Anomaly	$-26 \pm 1 \text{ }\mu\text{mol/kg}$	$-23 \pm 3 \text{ }\mu\text{mol/kg}$	$7 \pm 4 \text{ }\mu\text{mol/kg}$	$7 \pm 4 \text{ }\mu\text{mol/kg}$	$-18 \pm 1 \text{ }\mu\text{mol/kg}$	–	$-16 \pm 6 \text{ }\mu\text{mol/kg}$	–

Note. Columns missing data indicate that either the glacial or deglacial interval is defined by only one point. The most likely $[\text{CO}_3^{2-}]$ anomaly is listed for MIS 6/5e at 1,800 m, though the interglacial is defined by one point. See Section 3.2 for further discussion. Each error listed for the anomaly is the standard error based on averaging the glacial and deglacial points.

the sparsity of *C. wuellerstorfi* shells between 120 and 130 ka, the MIS 5e $[\text{CO}_3^{2-}]$ value is based on one data point at ~ 133 ka. The difference between this point and the MIS 6 average ($n = 3$) yields a $[\text{CO}_3^{2-}]$ decrease of $26 \pm 1 \mu\text{mol/kg}$, similar to that observed during HS1 at this depth (Lacerra et al., 2017). The TII $[\text{CO}_3^{2-}]$ signal is much smaller ($-15 \pm 4 \mu\text{mol/kg}$) if the three points near 135 ka are included, but these points do not represent full interglacial $[\text{CO}_3^{2-}]$ conditions. Regardless of which $[\text{CO}_3^{2-}]$ signal is used, the results clearly show negative carbonate ion anomalies occurred in both cores during TII, with the $[\text{CO}_3^{2-}]$ decline at 1,800 m leading the decline at 2,300 m by ~ 3 –5 ka.

The two cores show similar long-term $[\text{CO}_3^{2-}]$ trends during MIS 5 but contrasting behavior during the MIS 5d/c and 5b/a transitions. In both cores, $[\text{CO}_3^{2-}]$ remains low throughout MIS 5e, about $90 \mu\text{mol/kg}$ at 2,300 m and $85 \mu\text{mol/kg}$ at 1,800 m. At 2,300 m, negative $[\text{CO}_3^{2-}]$ anomalies occur at MIS 5d/c ($-18 \pm 1 \mu\text{mol/kg}$) and 5b/a. We refrain from calculating the magnitude of the MIS 5b/a anomaly because the deglacial interval consists of a single data point. At 1,800 m, there is no clear negative $[\text{CO}_3^{2-}]$ anomaly during MIS 5d/c, similar to the $\delta^{13}\text{C}$ record (Table 2). Instead, the $[\text{CO}_3^{2-}]$ record shows a slight positive anomaly. The MIS 5b/a transition also lacks a $[\text{CO}_3^{2-}]$ anomaly at 1,800 m. The $[\text{CO}_3^{2-}]$ trend appears to be positive but the low temporal resolution and high variability preclude any definitive statements about the trend. The absence of negative $[\text{CO}_3^{2-}]$ anomalies at 1,800 m during MIS 5 is likely because the core of NSW was located closer to 2,300 m (Shub et al., 2024).

The two $[\text{CO}_3^{2-}]$ time series show divergent patterns during MIS 4. At 2,300 m, $[\text{CO}_3^{2-}]$ decreased $26 \pm 6 \mu\text{mol/kg}$ from MIS 5a into MIS 4, reaching a minimum of $\sim 85 \mu\text{mol/kg}$. Benthic $\delta^{13}\text{C}$ at 2,300 m also decreased by $\sim 1\text{‰}$, reaching the lowest value in the entire record ($0.06 \pm 0.06\text{‰}$) (Figure 4). In contrast, $[\text{CO}_3^{2-}]$ and $\delta^{13}\text{C}$ remained relatively high at 1,800 m, with $[\text{CO}_3^{2-}]$ reaching its highest value throughout the record, though $[\text{CO}_3^{2-}]$ is variable throughout MIS 4. At the MIS 4/3 transition (59–62 ka), $[\text{CO}_3^{2-}]$ decreased by $16 \mu\text{mol/kg}$, paired with a decrease in $\delta^{13}\text{C}$ at 1,800 m, while at 2,300 m, $[\text{CO}_3^{2-}]$ increased, reaching a concentration similar to MIS 5a. Overall, our results show paired negative $[\text{CO}_3^{2-}]$ and $\delta^{13}\text{C}$ anomalies in at least one core during TII, MIS 5d/c, MIS 5b/a, and MIS 4/3.

4. Discussion

4.1. Evidence for AMOC Weakening During TI and TII

The similar timing and magnitude of $\delta^{13}\text{C}$ anomalies during TI and TII imply there was a common driving mechanism. Several ideas have been proposed to explain the $\delta^{13}\text{C}$ signal during TI, including: (a) greater brine formation in the Nordic Seas, which may impart a ^{13}C -depleted signature on NSW (Dokken & Jansen, 1999; Thornalley et al., 2010), (b) temperature-dependent equilibration with the atmospheric CO_2 (Lynch-Stieglitz et al., 1995, 2019), (c) greater incursion of low $\delta^{13}\text{C}$ Antarctic Intermediate Water (AAIW) (Rickaby & Elderfield, 2005), and (d) weakening of AMOC (Gu et al., 2021; Schmittner & Lund, 2015). Given that mid-depth (1,500–2,500 m) $\delta^{13}\text{C}$ anomalies lead those in the surface ocean and atmosphere, the atmospheric driver is unlikely (Lund et al., 2019). Evidence for reduced spatial extent of AAIW during the last deglaciation is also inconsistent with the $\delta^{13}\text{C}$ anomalies being caused by increased influence of AAIW (Xie et al., 2012). The most likely explanation is weakening of the AMOC; model results indicate that AMOC collapse causes accumulation of isotopically light respired carbon in the mid-depth Atlantic (Gu et al., 2021; Schmittner & Lund, 2015). Negative $\delta^{13}\text{C}$ anomalies are highly correlated with older ventilation ages, indicating that increased residence time of NSW allows for the accumulation of respired carbon (Gu et al., 2021).

If AMOC weakening also occurred during TII, we should observe negative B/Ca and $\delta^{13}\text{C}$ anomalies at the Brazil Margin. At 1,800 m, $[\text{CO}_3^{2-}]$ and $\delta^{13}\text{C}$ decreased by $\sim 26 \mu\text{mol/kg}$ and 0.46‰ , respectively (Table 2). At 2,300 m, $[\text{CO}_3^{2-}]$ decreased by $\sim 23 \mu\text{mol/kg}$, while there is no clear $\delta^{13}\text{C}$ anomaly. Therefore, the records at 1,800 m are consistent with AMOC weakening during TII. The lack of paired anomalies at 2,300 m is likely due to the shallower position of NSW during MIS 6, when the core of NSW, identifiable as a local maximum in vertical $\delta^{13}\text{C}$ profiles, was centered at $\sim 1,800$ m (Figure 5) (Curry & Oppo, 2005; Hoffman & Lund, 2012; Shub et al., 2024). The shallower core site is therefore better suited for recording changes in NSW during glacial terminations. Nonetheless, the record at 2,300 m shows a $[\text{CO}_3^{2-}]$ anomaly, which is likely due to changes in preformed dissolved inorganic carbon (DIC). Atmospheric pCO_2 concentration increased by ~ 90 ppm during TII, which would increase preformed DIC, resulting in lower $[\text{CO}_3^{2-}]$ at the Brazil Margin. At this time, the $\delta^{13}\text{C}$ of atmospheric pCO_2 decreased by only $\sim 0.1\text{‰}$ (Eggleston et al., 2016). Therefore, we would expect a clear signal

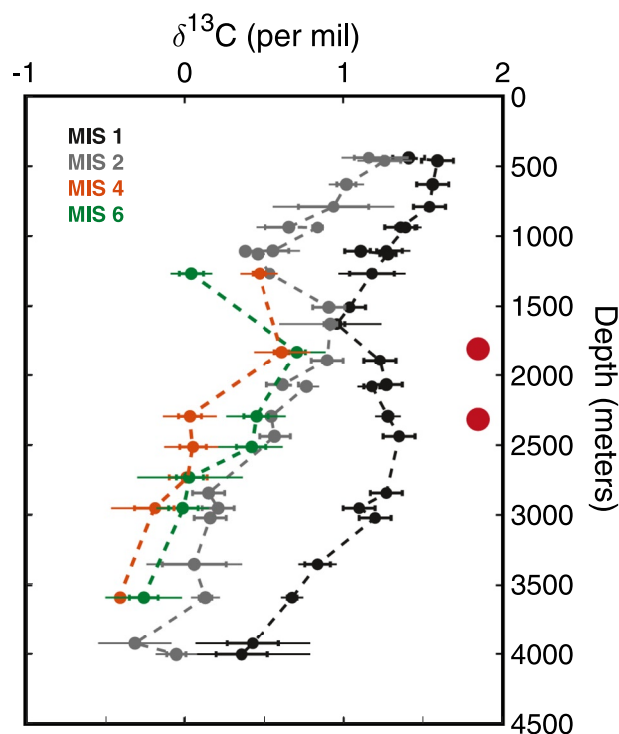


Figure 5. Brazil Margin vertical $\delta^{13}\text{C}$ profiles for MIS 1 (Holocene), MIS 2 (Last Glacial Maximum), MIS 4, and MIS 6. Circles represent the mean $\delta^{13}\text{C}$ for each time period, horizontal bars represent $\pm 1\sigma$ uncertainty, vertical notches represent $\pm 1\text{SE}$. Data from Curry and Oppo (2005), Hoffman and Lund (2012), and Shub et al. (2024). Red circles note the depth of the two cores used in this study (shallower core is 79JPC, deeper core is 42JPC).

in $[\text{CO}_3^{2-}]$ and little change in $\delta^{13}\text{C}$, consistent with the results at 2,300 m. The initial decrease in $[\text{CO}_3^{2-}]$ at 2,300 m lags the shift in $[\text{CO}_3^{2-}]$ at 1,800 m by 3–5 kyr, suggesting that weakening of the AMOC first caused the anomaly at 1,800 m, followed by changes in preformed DIC at 2,300 m as atmospheric pCO_2 rose.

Published evidence indicates the AMOC was suppressed for a longer, uninterrupted interval during TII, without the temporary recovery observed during TI. Sortable silt, $^{231}\text{Pa}/^{230}\text{Th}$, and ϵ_{Nd} data imply the AMOC remained weak throughout Heinrich Stadial 11 (Böhm et al., 2015; Deaney et al., 2017; Hodell et al., 2009). Several mechanisms have been proposed to explain the differences between TI and TII. Greater summertime insolation forcing during TII likely drove ice sheet melt and rapid sea level rise, contributing to greater freshwater forcing and a longer period of AMOC suppression (Carlson, 2008) (Figure 6). This may have been particularly important during the late stages of TII (Obase et al., 2021). In addition, a larger Eurasian ice sheet during the last interglacial period may have supplied additional meltwater at the beginning of TII (Clark et al., 2020). AMOC collapse likely causes subsurface warming in the North Atlantic, which would destabilize grounding lines and ice shelves, causing more rapid ice sheet retreat (Alvarez-Solas et al., 2011; Clark et al., 2007, 2020; Marcott et al., 2011; Shaffer et al., 2004). Thus, sustained AMOC weakening during TII was likely due to a positive feedback between ocean circulation, ice shelf destabilization, and ice sheet melt.

Spatial patterns in $[\text{CO}_3^{2-}]$ within the Atlantic can also be used to assess AMOC behavior during TII. AMOC weakening results in greater accumulation of respired carbon in the North Atlantic than the South Atlantic, a spatial gradient that can be detected using $[\text{CO}_3^{2-}]$ (Gu et al., 2021; Schmittner & Lund, 2015). During HS1, for example, $[\text{CO}_3^{2-}]$ decreased by 29 $\mu\text{mol/kg}$ in the tropical North Atlantic and by approximately 22 $\mu\text{mol/kg}$ at the Brazil Margin (Lacerra et al., 2017; Yu et al., 2010). Similarly, during TII, $[\text{CO}_3^{2-}]$ in the tropical North Atlantic declined 34 $\mu\text{mol/kg}$ (Yu et al., 2013), while

the decline at the Brazil Margin was 26 $\mu\text{mol/kg}$. During both terminations, the North Atlantic $[\text{CO}_3^{2-}]$ change is $\sim 30\%$ larger than at the Brazil Margin, consistent with the modeled spatial pattern of DIC anomalies in the Atlantic basin (Gu et al., 2021; Schmittner & Lund, 2015).

The preceding discussion assumes that DIC is the primary driver of the down-core $[\text{CO}_3^{2-}]$ variability. But $[\text{CO}_3^{2-}]$ is also affected by alkalinity ($[\text{CO}_3^{2-}] \approx 0.6 * (\text{ALK} - \sum \text{CO}_2)$) (Yu et al., 2016). Model simulations imply AMOC collapse causes an alkalinity response of approximately +20 $\mu\text{M/kg}$ at the Brazil Margin, due to a more sluggish overturning and accumulation of $[\text{Ca}^{2+}]$ from the hard tissue pump (Lacerra et al., 2017; Schmittner & Lund, 2015). Such a change would cause higher $[\text{CO}_3^{2-}]$ and result in an underestimate of the DIC signal. Rising sea level would facilitate carbonate deposition on shelves, which would decrease open ocean alkalinity and therefore $[\text{CO}_3^{2-}]$. Carbonate deposition likely had little impact on the TI $[\text{CO}_3^{2-}]$ signal given that the majority of sea level rise occurred after HS1, but it may have been a factor during TII, when sea level rose by ~ 80 m during the weakened AMOC interval of TII (Figure 6). Given that carbonate precipitation has little effect on the $\delta^{13}\text{C}$ of DIC (Maslin & Swann, 2006), the synchronous $\delta^{13}\text{C}$ anomalies would require a separate explanation. While we cannot rule out a sea level driver of the $[\text{CO}_3^{2-}]$ signal, the simpler explanation for coherent changes in $[\text{CO}_3^{2-}]$ and $\delta^{13}\text{C}$ is the accumulation of isotopically light respired carbon due to AMOC collapse.

4.2. Evidence for AMOC Weakening During the MIS 5 Deglaciations

Negative $\delta^{13}\text{C}$ and $[\text{CO}_3^{2-}]$ anomalies at 2,300 m indicate AMOC weakening occurred during the MIS 5d/c and 5b/a transitions. The lack of paired $\delta^{13}\text{C}$ and $[\text{CO}_3^{2-}]$ anomalies at 1,800 m is most likely due to deepening of NSW during MIS 5. Vertical profiles of $\delta^{13}\text{C}$ from the Brazil Margin indicate the core of NSW deepened from $\sim 1,800$ m during MIS 6 to $\sim 2,500$ m during MIS 5 (Shub et al., 2024), similar to the transition from MIS 2 to MIS 1 (Figure 5). As a result, the core at 2,300 m would have been heavily influenced by NSW, allowing it

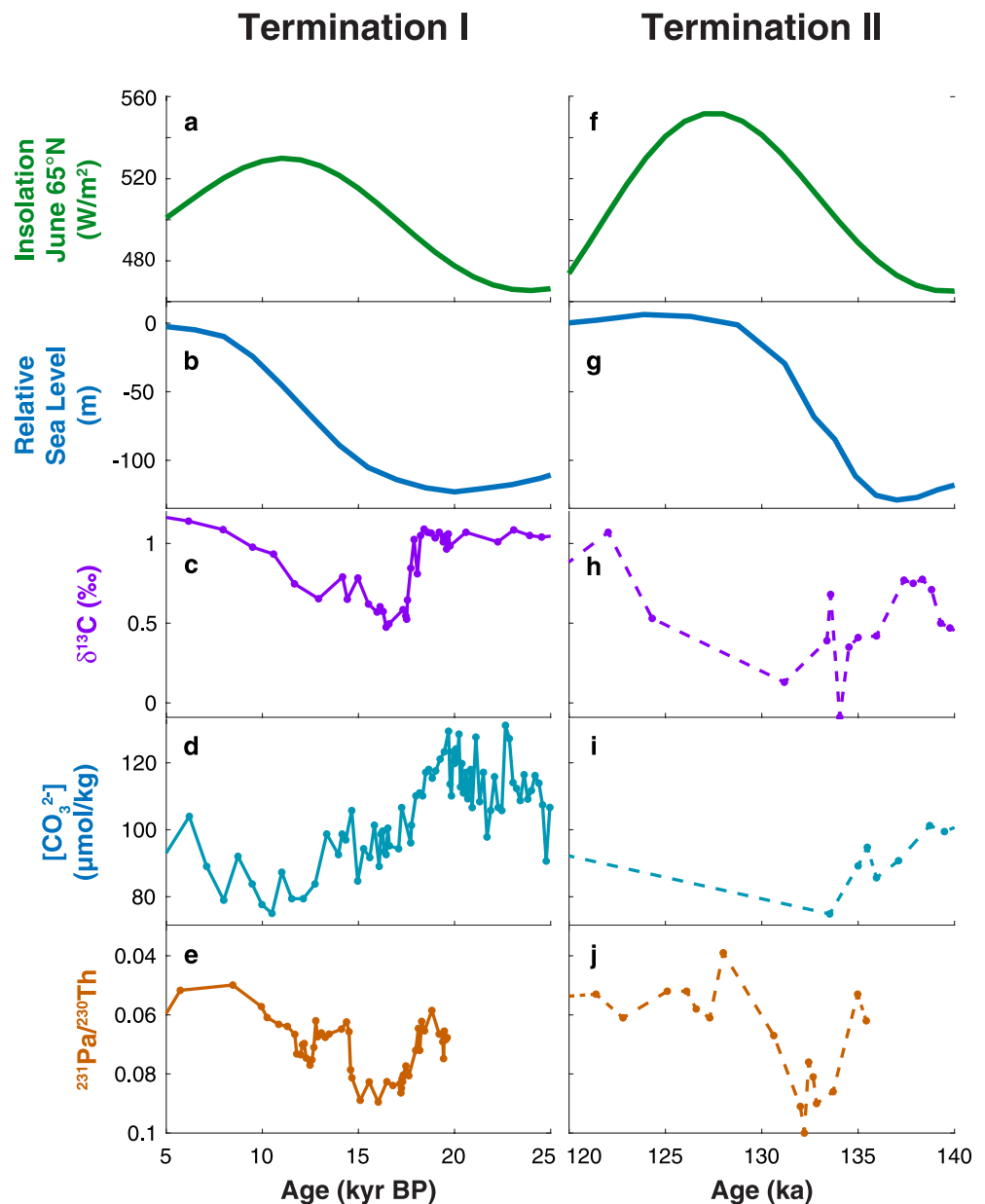


Figure 6. Comparison of records for Termination I (TI) (a)–(e) and Termination II (TII) (f)–(j). (a, f) June 21, 65°N insolation (Laskar et al., 2004; Tzedakis et al., 2017). (b, g) Relative sea level (Waelbroeck et al., 2002). (c, h) $\delta^{13}\text{C}$ at 1,800 m at the Brazil Margin, with TI data from Tessin and Lund (2013) and TII data from this study. (d, i) $[\text{CO}_3^{2-}]$ derived from foraminiferal B/Ca at 1,800 m on the Brazil Margin, with TI data from Lacerra et al. (2017) and TII data from this study. (e, j) $^{231}\text{Pa}/^{230}\text{Th}$ from the Bermuda Rise, including data for TI (McManus et al., 2004) and TII (Böhm et al., 2015).

to better capture changes in AMOC variability. The clear depth-sensitivity at the Brazil Margin highlights the importance of using multiple cores to assess the influence of NSW position on proxy time series.

While $\delta^{13}\text{C}$ and $[\text{CO}_3^{2-}]$ results at 1,800 m lack clear evidence for AMOC weakening during the MIS 5b/a transition, there is a negative $\delta^{13}\text{C}$ anomaly at this time. During the transition, benthic $\delta^{13}\text{C}$ shifted to lower values, but $\delta^{13}\text{C}$ remained low for the duration of MIS 5a (~15 kyr), much longer than the MIS 5d/c and 5b/a $\delta^{13}\text{C}$ anomalies at 2,300 m (Figure 4). Low $\delta^{13}\text{C}$ values at 1,800 m during MIS 5a may have been caused by a slight deepening of NSW (Shub et al., 2024). In this scenario, we would also expect lower $[\text{CO}_3^{2-}]$, however, which is not apparent in the record. Further work is needed to identify the cause of this apparent discrepancy, including detailed $[\text{CO}_3^{2-}]$ records across a range of water depths. Despite the ambiguous MIS 5a data at 1,800 m, the $\delta^{13}\text{C}$ and $[\text{CO}_3^{2-}]$

results at 2,300 m, where the core of NSW was located during MIS 5, are consistent with AMOC weakening during the MIS 5d/c and MIS 5b/a transitions.

In addition to AMOC strength and watermass geometry, the $[\text{CO}_3^{2-}]$ records are also influenced by glacial-interglacial changes in atmospheric pCO_2 . After TII, when the AMOC presumably strengthened, the Brazil Margin $[\text{CO}_3^{2-}]$ records do not fully recover to pre-TII values (Figure 4). Persistently low $[\text{CO}_3^{2-}]$ was likely caused by higher atmospheric pCO_2 during MIS 5e, which increases the preformed [DIC] of NSW. A similar pattern is observed during TI, when $[\text{CO}_3^{2-}]$ at 1,800 m and 2,100 m remained low into the early Holocene (Lacerra et al., 2017). The pattern following terminations is in contrast to the smaller deglaciations of MIS 5, where there is little delay in $[\text{CO}_3^{2-}]$ recovery. The difference is most likely due to the small increases in atmospheric pCO_2 of ~10–20 ppm during MIS 5d/c and 5b/a, compared to the ~90 ppm increase during TII (Figure 1) (Bereiter et al., 2015). Once AMOC recovers after smaller deglaciations, $[\text{CO}_3^{2-}]$ quickly returns to glacial values because there is little change in preformed [DIC].

4.3. Relationship Between Insolation and AMOC Weakening

It is well-known that changes in insolation pace deglaciations (Hays et al., 1976; Huybers & Wunsch, 2005). How the climate system translates insolation variability into the disintegration of Northern Hemisphere ice sheets is far less clear, however. If AMOC weakening plays a central role in deglaciations (Cheng et al., 2009, 2016), there should be a predictable relationship between insolation and proxies of AMOC strength. As shown in Figure 7, $\delta^{13}\text{C}$ anomalies at the Brazil Margin occur when the rate of change in boreal summertime insolation is highest. These results strongly indicate insolation paces deglaciations via the AMOC. We suggest that ice sheet meltwater forced AMOC weakening and the resulting sub-surface warming accelerated deglaciation through melting of ice shelves and destabilization of grounding lines. We refer to this positive feedback as the AMOC trigger, where initial AMOC weakening can drive the ice sheet disintegration through oceanic forcing.

If insolation-driven changes in AMOC strength are key drivers of deglaciation, why doesn't increasing boreal summertime insolation always result in a termination? The most likely explanation is that large ice sheets are required for the AMOC trigger to be effective. Several authors have suggested that the Laurentide Ice Sheet needs to be large in order to predispose it to collapse once insolation rises (Abe-Ouchi et al., 2013; Cheng et al., 2009; Eggleston et al., 2016; Parrenin & Paillard, 2003). Given the apparent feedback between AMOC weakening and ice sheet melt, larger and isostatically adjusted ice sheets with grounding lines and extended ice shelves may be necessary to pre-condition the climate system for terminations, making an ice sheet more vulnerable to collapse, thereby providing a larger, more sustained meltwater event to keep the AMOC suppressed. Consistent with this idea, we observe evidence for AMOC weakening during MIS 5d/c and 5b/a, yet the lack of large Northern Hemisphere ice sheets likely limited the impact of the AMOC trigger mechanism, thereby preventing full ice sheet retreat.

Model results also indicate rising atmospheric pCO_2 is required to reach a full termination (Shakun et al., 2012). One possibility is that AMOC weakening caused enhanced Southern Ocean upwelling and outgassing of CO_2 through a poleward shift in the Southern Hemisphere westerlies (Anderson et al., 2009) or through weakening of the biological pump (Hertzberg et al., 2016). In the latter case, simulated AMOC weakening reduces upwelling of nutrients to the surface ocean, which in turn reduces biological export of carbon, resulting in higher surface ocean and atmospheric pCO_2 (Schmittner, 2005; Schmittner & Lund, 2015). The magnitude or duration of AMOC weakening required to trigger these feedbacks is unclear, but both may play a role in regulating atmospheric pCO_2 during terminations.

While passive tracers such as $\delta^{13}\text{C}$ and $[\text{CO}_3^{2-}]$ are unable to directly constrain AMOC strength, dynamical proxies can be used to assess relative changes in magnitude. $^{231}\text{Pa}/^{230}\text{Th}$ records for the last glacial cycle indicate AMOC collapse occurred near glacial maxima, with values approaching the production ratio (0.093) (Böhm et al., 2015; McManus et al., 2004). Smaller $^{231}\text{Pa}/^{230}\text{Th}$ anomalies during the MIS 5d/c and 5b/a transitions are consistent with AMOC weakening, but not a full collapse (Figure 7) (Böhm et al., 2015). The timing of $^{231}\text{Pa}/^{230}\text{Th}$ anomalies is consistent with $\delta^{13}\text{C}$ anomalies at the Brazil Margin, providing additional evidence of AMOC weakening during each deglaciation of the last 150 ka. The positive shift in $^{231}\text{Pa}/^{230}\text{Th}$ at the MIS 4/3 transition also suggests this deglaciation was characterized by a weaker AMOC, consistent with the $\delta^{13}\text{C}$ anomaly at 1,800 m (Figure 7). The difference in magnitude of AMOC weakening between MIS 5 and glacial maxima supports the idea that large ice sheets are required for the AMOC trigger to effectively drive a full termination.

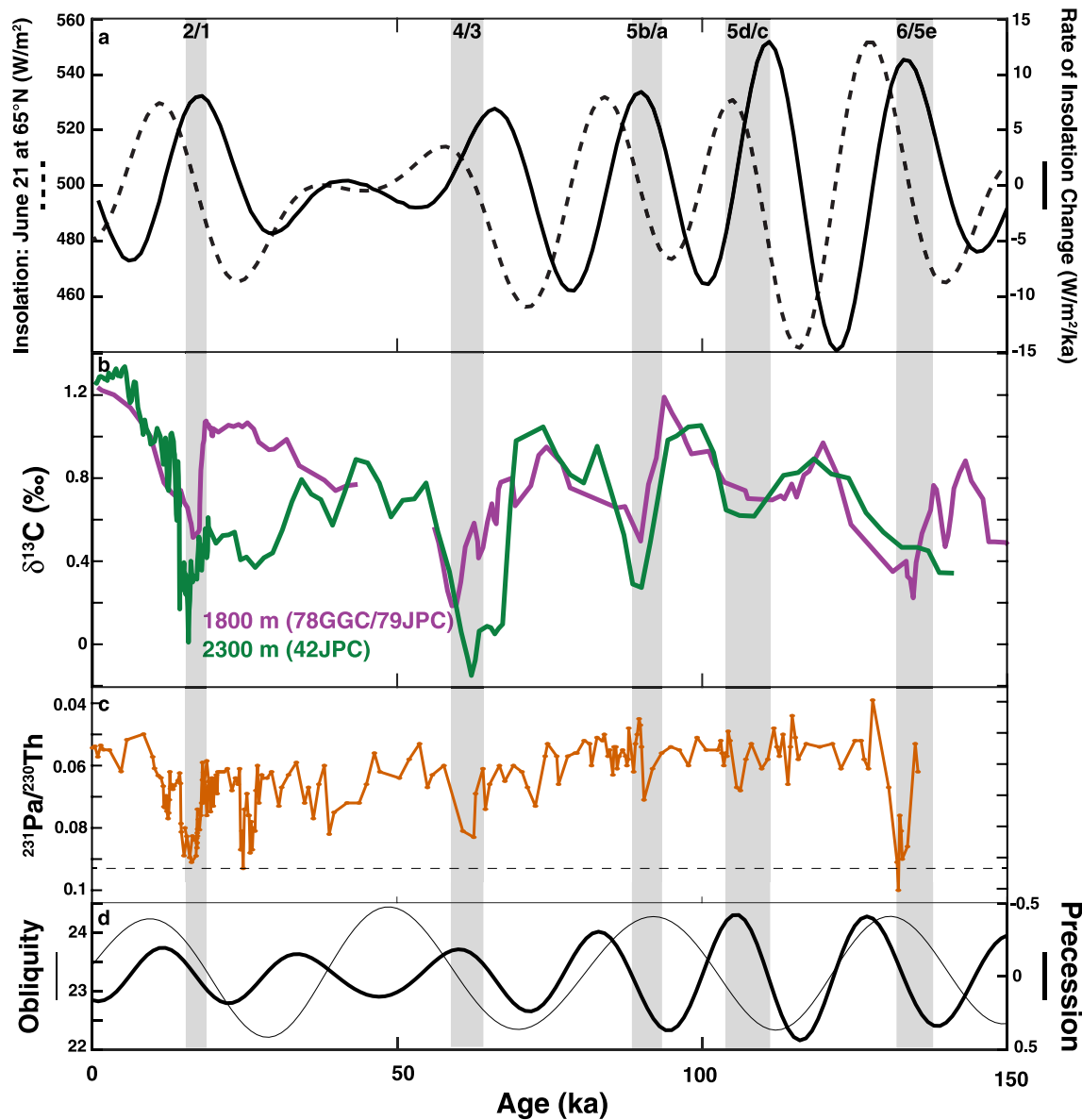


Figure 7. Atlantic overturning circulation proxies compared to Northern Hemisphere summertime insolation and orbital parameters. (a) June 21 insolation at 65°N (dashed line) and rate of insolation change (solid line) (Laskar et al., 2004; Tzedakis et al., 2017). (b) Benthic $\delta^{13}\text{C}$ results from 1,800 to 2,300 m, plotted as a simple three-point running average. At 1,800 m, the 0–40 ka data is from core KNR159-5-78GGC, the companion gravity core to 79JPC which makes up the data from 50 to 150 ka. (c) $^{231}\text{Pa}/^{230}\text{Th}$ at ~4,500 m on the Bermuda Rise (Böhm et al., 2015; Lippold et al., 2009; McManus et al., 2004). Dashed line is the $^{231}\text{Pa}/^{230}\text{Th}$ production ratio (0.093). (d) Precession ($\epsilon \sin(\omega)$; thick line) and obliquity (degrees; thin line) (Laskar et al., 2004). Note right-hand y-axis is inverted so June perihelion is upwards. Gray vertical bars highlight negative $\delta^{13}\text{C}$ anomalies on deglaciations. Comparison with the caloric summer 65°N insolation curve (Tzedakis et al., 2017) yields the same temporal relationship between insolation and $\delta^{13}\text{C}$.

The relationship between insolation and AMOC strength over the last 150 ka raises the question of whether a similar link occurs over longer timescales. Lisiecki et al. (2008) explored the relationship between Milankovitch forcing and Atlantic overturning using a compilation of $\delta^{13}\text{C}$ records from the Atlantic and Pacific spanning the last 425 ka. The strength/depth of NSW was inferred using the mixing ratio between NSW and Southern Source Water (SSW), or $\Delta\delta^{13}\text{C}$, which was calculated by averaging North Atlantic records between 3,000 and 4,000 m and subtracting the average $\delta^{13}\text{C}$ of Pacific records (assumed to represent mean ocean $\delta^{13}\text{C}$). Similar to our results from the Brazil Margin, Lisiecki et al. (2008) found that low $\Delta\delta^{13}\text{C}$, or reduced NSW influence, coincided with maximum Milankovitch forcing in the precession band. But they also found that maximum obliquity forcing is associated with *greater* $\Delta\delta^{13}\text{C}$ (i.e., enhanced overturning), in contrast to earlier work that found a consistent

ocean circulation response in the precession and obliquity bands (Imbrie et al., 1992). Lisiecki (2014) extended the data compilation to 3 Ma and found similar results for the last 1.5 Ma. Here we suggest that high $\Delta\delta^{13}\text{C}$ associated with obliquity maxima are due to deepening of NSW, which would enrich ^{13}C in the 3,000–4,000 m depth range. At shallower sites (e.g., 1,800 m at the Brazil Margin), $\delta^{13}\text{C}$ minima occur during the obliquity maxima of TI and TII, implying that AMOC consistently weakens due to Milankovitch forcing in both the precession and obliquity bands (Figure 7). A full evaluation of AMOC response to insolation forcing will require longer time-series partitioned into depth ranges that account for the change in water mass structure over glacial-interglacial cycles.

4.4. MIS 4

The Brazil Margin $\delta^{13}\text{C}$ and $[\text{CO}_3^{2-}]$ records indicate there was increased carbon storage in the deep Atlantic during MIS 4. At 2,300 m, large decreases in both $[\text{CO}_3^{2-}]$ and $\delta^{13}\text{C}$ during the MIS 5/4 transition are consistent with accumulation of respired carbon below 2 km water depth (Figure 4). The increase in $[\text{CO}_3^{2-}]$ at 1,800 m during the MIS 5/4 transition is in stark contrast to the results at 2,300 m. Shifting of nutrients and respired carbon from the intermediate to deep Atlantic could explain the opposing trends at 1,800 and 2,300 m (Boyle, 1988; Yu et al., 2013). The Brazil Margin $\delta^{13}\text{C}$ vertical profile for MIS 4 suggests the NSW/SSW boundary shoaled to ~2,000 m, the shallowest position of the last glacial cycle (Figure 5) (Shub et al., 2024). Widespread decreases in Atlantic $\delta^{13}\text{C}$ below 2,000 m imply there was reduced ventilation of abyssal Atlantic, perhaps due to displacement of NSW by SSW (Kohfeld & Chase, 2017; Oliver et al., 2010). Results from the ϵ_{Nd} tracer are consistent with greater influence of SSW in the deep South Atlantic (Piotrowski et al., 2005; Wilson et al., 2015), further highlighting the unique nature of MIS 4 in the Atlantic basin.

Several mechanisms have been proposed to explain the MIS 4 shift in deep ocean circulation. Northward migration of the Southern Hemisphere westerly winds may have decreased upwelling of deep waters in the Southern Ocean, enhancing carbon storage in the deep Atlantic (Toggweiler, 1999). Alternatively, decreased surface temperatures in the North Atlantic would have cooled NSW, which upon reaching the coast of Antarctica may have reduced melting of land ice, which would yield a colder, saltier deep SSW and enhanced stratification of the deep Atlantic (Adkins, 2013). Or expanded sea ice coverage in the Southern Ocean may have caused shoaling of the NSW/SSW boundary, which tends to reduce mixing between the two watermasses (Ferrari et al., 2014). A shoaled water mass boundary during the MIS 5/4 transition would allow the 2,300 m core site to be influenced by the “deep” waters which were presumably sequestering DIC, resulting in the large $\delta^{13}\text{C}$ and $[\text{CO}_3^{2-}]$ anomalies, while the shallower site continued to be influenced primarily by NSW.

Enhanced carbon storage in the deep Atlantic likely contributed to the large (~40 ppm) decrease in atmospheric pCO_2 during the MIS 5/4 transition (Figure 1). Enhanced solubility of CO_2 due to lower global mean SSTs (Kohfeld & Chase, 2017; Snyder, 2016) played a relatively small role in the atmospheric pCO_2 drawdown (Shackleton et al., 2021). Accumulation of respired carbon and slower deep water ventilation likely explain the large $\delta^{13}\text{C}$ and $[\text{CO}_3^{2-}]$ changes at 2,300 m. Using the relationship $\text{DIC} \approx \text{ALK} - [\text{CO}_3^{2-}]/0.6$ (Yu et al., 2016), the decrease in $[\text{CO}_3^{2-}]$ of $26 \pm 6 \mu\text{mol/kg}$ at 2,300 m would equate to an increase in [DIC] of $\sim 43 \mu\text{mol/kg}$. Large negative $[\text{CO}_3^{2-}]$ anomalies occurred in several deep (3,000–5,000 m) Atlantic sites at the MIS 5/4 transition (Yu et al., 2016) (Figure 8). Data from the deep Atlantic compilation imply [DIC] increased $42 \pm 22 \mu\text{mol/kg}$, similar to our estimate from the Brazil Margin. Yu et al. (2016) estimate that the deep Atlantic stored $\sim 86 \pm 56\%$ of the total CO_2 drawdown across the MIS 5/4 transition. Our result from 2,300 m suggests this is a conservative estimate, given that our site is located shallower in the water column. Thus, it appears that the deep Atlantic served as an important sink for atmospheric CO_2 during the last glacial cycle, with the Brazil Margin records indicating carbon storage occurred below 2 km water depth.

Given that $[\text{CO}_3^{2-}]$ is affected by both [DIC] and alkalinity, it is important to consider whether alkalinity contributed to the MIS 5/4 $[\text{CO}_3^{2-}]$ signal. Sea level decreased by ~50 m during the MIS 5/4 transition (Spratt & Lisiecki, 2016; Waelbroeck et al., 2002), which would have decreased neritic carbonate production and led to higher oceanic alkalinity (Milliman, 1993). In addition, carbon sequestration in the deep Atlantic would have caused acidification and dissolution of seafloor calcium carbonate, resulting in a temporary imbalance between inputs and outputs of alkalinity to the ocean. Carbonate compensation would have worked to bring the system back to steady state by raising alkalinity through CaCO_3 dissolution, thereby raising $[\text{CO}_3^{2-}]$ to its pre-perturbation levels, on a timescale of 5–7 kyr (Broecker & Peng, 1987; Sigman & Boyle, 2000; Yu et al., 2014, 2016). At

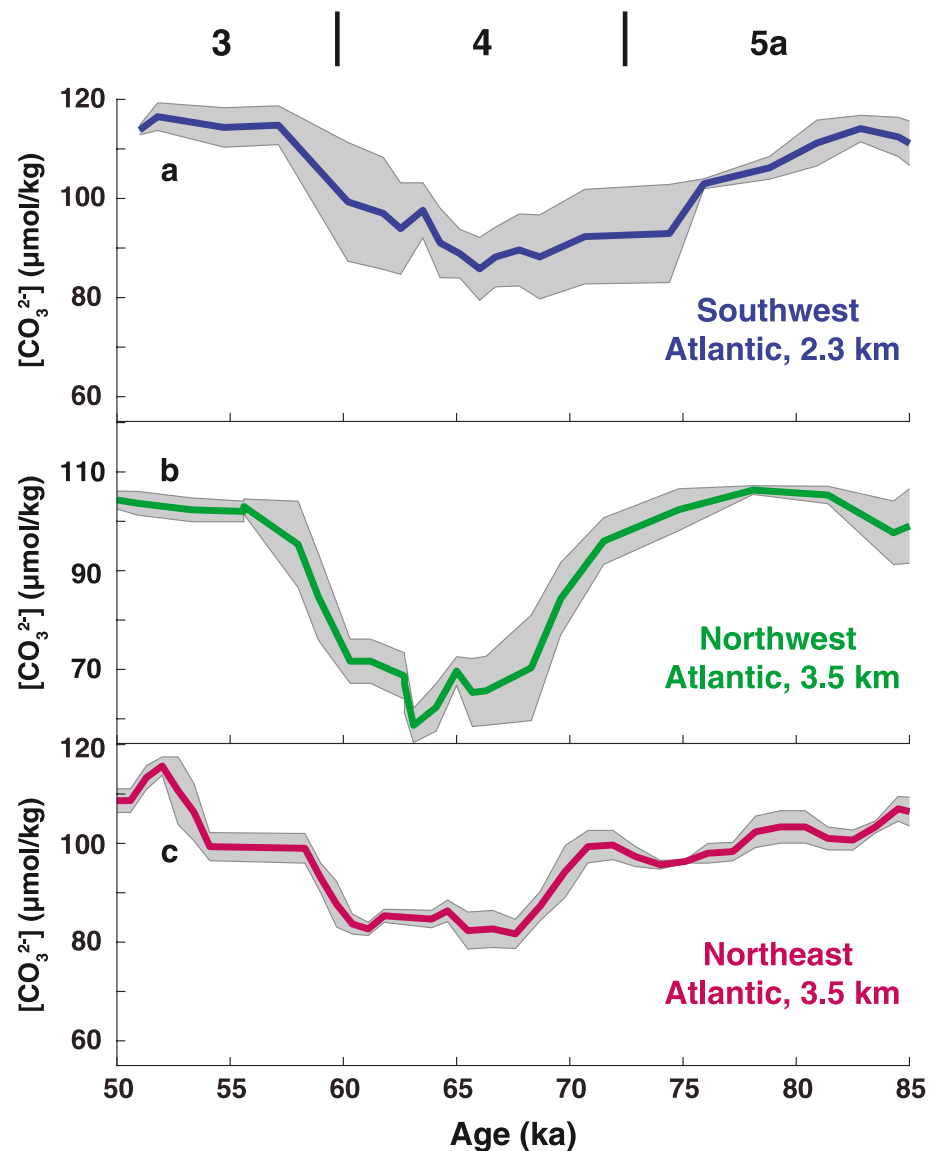


Figure 8. Reconstructions of $[\text{CO}_3^{2-}]$ across the MIS 5a–4–3 transitions at three Atlantic core sites. (a) $[\text{CO}_3^{2-}]$ record from 2,300 m at the Brazil Margin (this study), (b) 3,500 m in the Northwest Atlantic (4°N, 43°W; Yu et al., 2016), and (c) and 3,600 m in the Northeast Atlantic (39°N, 12.6°W; Yu et al., 2016). In each case, the data are presented as a simple three-point running average (solid line) with standard error (gray envelope). Approximate timing of marine isotope stages are shown at top.

the Brazil Margin, $[\text{CO}_3^{2-}]$ at 2,300 m remained low throughout MIS 4, similar to the pattern in other deep Atlantic locations (Figure 8). Persistently low $[\text{CO}_3^{2-}]$ values suggest alkalinity had little impact on deep Atlantic $[\text{CO}_3^{2-}]$. The anticipated alkalinity signal may have been balanced by a reduction in riverine alkalinity flux or higher alkalinity in the Indo-Pacific (Yu et al., 2016). The alkalinity budget may have been partially balanced through changes in the upper Atlantic. At 1,800 m, we observe a $\sim 10 \mu\text{mol/kg}$ increase in $[\text{CO}_3^{2-}]$ during MIS 4 (Figure 4), possibly due to a positive alkalinity response. An increase in ocean alkalinity due to CaCO_3 dissolution would drive further atmospheric CO_2 drawdown (Boyle, 1988). Additional $[\text{CO}_3^{2-}]$ records are necessary to verify whether the signal we observe at the Brazil Margin is representative of the entire upper Atlantic.

Results from the Brazil Margin are consistent with AMOC weakening across the MIS 4/3 deglaciation. At 1,800 m, $\delta^{13}\text{C}$ decreased by 0.36‰ and $[\text{CO}_3^{2-}]$ decreased by $16 \mu\text{mol/kg}$ (Figure 4). Vertical profiles of $\delta^{13}\text{C}$ and $\delta^{18}\text{O}$ suggest the NSW/SSW boundary was located at approximately 2,000 m during MIS 4, its shallowest depth

of the last glacial cycle (Shub et al., 2024) (Figure 5). We should therefore expect to see clear $\delta^{13}\text{C}$ and $[\text{CO}_3^{2-}]$ anomalies at 1,800 m associated with AMOC collapse (Table 2). Higher $^{231}\text{Pa}/^{230}\text{Th}$ values near the end of MIS 4 are also consistent with AMOC weakening during the MIS 4/3 deglaciation (Böhm et al., 2015) (Figure 7). The pronounced shifts in deep Atlantic circulation and carbon cycling that occurred during MIS 4 make it difficult to identify any signs of AMOC weakening at 2,300 m. There is a small but distinct decrease in $\delta^{13}\text{C}$ at the MIS 4/3 transition (Figure 4), but overall low background $\delta^{13}\text{C}$ values may have masked the full magnitude of any AMOC-related signal. Variability in the $[\text{CO}_3^{2-}]$ signal also precludes identification of clear anomalies (Figure 4). Furthermore, increased whole ocean alkalinity due to oceanic carbon uptake and acidification may also obscure any $[\text{CO}_3^{2-}]$ signal associated with AMOC variability. Overall, however, we believe the main reason for more pronounced $\delta^{13}\text{C}$ and $[\text{CO}_3^{2-}]$ anomalies at 1,800 m at the MIS 4/3 transition is shoaling of NSW during the preceding glacial interval, similar to the pattern during TII.

5. Conclusions

The cause of Pleistocene deglaciations remains poorly understood, highlighting our incomplete understanding of Earth's climate system. While it has long been known that insolation paces glacial-interglacial cycles (Hays et al., 1976; Imbrie et al., 1992), the exact mechanisms by which insolation drives disintegration of Northern Hemisphere ice sheets remain poorly constrained. One hypothesis is that insolation-driven melting of continental ice weakens the AMOC through freshwater forcing, which in turn causes sub-surface oceanic warming, thinning of ice shelves, and retreat of ice sheet grounding lines (Alvarez-Solas et al., 2011; Clark et al., 2020; Marcott et al., 2011). Evidence for AMOC weakening exists for the last two glacial terminations (Böhm et al., 2015; Lacerra et al., 2017; McManus et al., 2004; Oppo et al., 1997), when ice volume, sea level, and atmospheric CO_2 were at comparable levels (Bereiter et al., 2015; Lisiecki & Stern, 2016; Waelbroeck et al., 2002). But a key test of the AMOC-driver hypothesis is whether weakening occurred across a range of climate states, such as the smaller deglaciations of MIS 5.

Here we present reconstructions of AMOC variability for the last 150 ka, a time interval that includes glacial maxima (MIS 2 and 6) and intermediate glacial conditions (MIS 4, 5b and 5d). We infer AMOC strength using benthic foraminiferal estimates of $\delta^{13}\text{C}$ and $[\text{CO}_3^{2-}]$ from two cores at the Brazil Margin, located at 1,800 m and 2,300 m water depth. We find evidence for negative $\delta^{13}\text{C}$ or $[\text{CO}_3^{2-}]$ anomalies during each deglaciation, which are most easily explained by AMOC weakening and accumulation of respired carbon in the mid-depth Atlantic (1,500–2,500 m) (Gu et al., 2021; Lacerra et al., 2017; Schmittner & Lund, 2015). The respired carbon signal varies with depth, with the shallower core showing the most pronounced anomalies during TI, TII, and the MIS 4/3 deglaciation and the deeper core having larger anomalies during the MIS 5d/c and 5b/a deglaciations. The difference between the two sites reflects shoaling of NSW during glacial intervals (MIS 2, 4, and 6) and deepening during the last interglacial interval (MIS 5). Combined with published $^{231}\text{Pa}/^{230}\text{Th}$ data from the North Atlantic (Böhm et al., 2015; McManus et al., 2004), our results highlight weakening of the AMOC during each deglaciation of the last 150 ka.

Our results indicate deglacial AMOC weakening occurred during a range of different boundary conditions, most likely due to increasing Northern Hemisphere summertime insolation and meltwater input to the North Atlantic. Prior studies based on deep Atlantic $\delta^{13}\text{C}$ records (2,300–4,000 m) found different phasing between maximum Milankovitch forcing and AMOC strength in the obliquity and precession bands (Lisiecki, 2014; Lisiecki et al., 2008). The $\delta^{13}\text{C}$ and $[\text{CO}_3^{2-}]$ records presented here suggest that the dynamic position of NSW on glacial-interglacial timescales complicates the phasing between Milankovitch forcing and proxies of Atlantic overturning. Vertical profiles of $\delta^{13}\text{C}$, $\delta^{18}\text{O}$, and $[\text{CO}_3^{2-}]$ for the last glacial cycle are necessary to better constrain the position of NSW for MIS 1 to 6 and to evaluate the remineralized carbon signal at a range of water depths. Combined with longer records of $\delta^{13}\text{C}$, it will be possible to fully assess AMOC response to orbital forcing across a range of timescales.

Data Availability Statement

The Brazil Margin B/Ca data presented here are available from the National Oceanic and Atmospheric Administration's Paleoclimatology Data service (Garity & Lund, 2023). The Brazil Margin stable isotope data presented here are available from the National Oceanic and Atmospheric Administration's Paleoclimatology Data service (Shub et al., 2023).

Acknowledgments

We would like to thank Lora Wingate and Kacey Lohmann for their help with stable isotope analyses. We would also like to thank Sarah McCart for assistance with the ICP-MS analyses and the WHOI core lab for sample collection and archiving. This work was supported by NSF Grant OCE-1804030 and the University of Connecticut Graduate School Harriott Fellowship.

References

- Abe-Ouchi, A., Saito, F., Kawamura, K., Raymo, M. E., Okuno, J., Takahashi, K., & Blatter, H. (2013). Insolation-driven 100,000-year glacial cycles and hysteresis of ice-sheet volume. *Nature*, 500(7461), 190–193. <https://doi.org/10.1038/nature12374>
- Adkins, J. F. (2013). The role of deep ocean circulation in setting glacial climates. *Paleoceanography*, 28(3), 539–561. <https://doi.org/10.1002/palo.20046>
- Ahn, J., & Brook, E. J. (2014). Siple Dome ice reveals two modes of millennial CO₂ change during the last ice age. *Nature Communications*, 5(1), 3723. <https://doi.org/10.1038/ncomms4723>
- Alvarez-Solas, J., Montoya, M., Ritz, C., Ramstein, G., Charbit, S., Dumas, C., et al. (2011). Heinrich event 1: An example of dynamical ice-sheet reaction to oceanic changes. *Climate of the Past*, 7(4), 1297–1306. <https://doi.org/10.5194/cp-7-1297-2011>
- Anderson, R. F., Ali, S., Bradtmiller, L. I., Nielsen, S. H. H., Fleisher, M. Q., Anderson, B. E., & Burckle, L. H. (2009). Wind-driven upwelling in the southern ocean and the deglacial rise in atmospheric CO₂. *Science*, 323(5920), 1443–1448. <https://doi.org/10.1126/science.1167441>
- Bereiter, B., Eggleston, S., Schmitt, J., Nehrass-Ahles, C., Stocker, T. F., Fischer, H., et al. (2015). Revision of the EPICA Dome C CO₂ record from 800 to 600 kyr before present. *Geophysical Research Letters*, 42(2), 542–549. <https://doi.org/10.1002/2014GL061957>
- Bereiter, B., Lüthi, D., Siegrist, M., Schüpbach, S., Stocker, T. F., & Fischer, H. (2012). Mode change of millennial CO₂ variability during the last glacial cycle associated with a bipolar marine carbon seesaw. *Proceedings of the National Academy of Sciences of the United States of America*, 109(25), 9755–9760. <https://doi.org/10.1073/pnas.1204069109>
- Böhm, E., Lippold, J., Gutjahr, M., Frank, M., Blaser, P., Antz, B., et al. (2015). Strong and deep Atlantic meridional overturning circulation during the last glacial cycle. *Nature*, 517(7532), 73–76. <https://doi.org/10.1038/nature14059>
- Boyle, E. A. (1988). The role of vertical chemical fractionation in controlling late Quaternary atmospheric carbon dioxide. *Journal of Geophysical Research*, 93(C12), 15701–15714. <https://doi.org/10.1029/JC093iC12p15701>
- Broecker, W. S., & Peng, T. (1987). The role of CaCO₃ compensation in the glacial to interglacial atmospheric CO₂ change. *Global Biogeochemical Cycles*, 1(1), 15–29. <https://doi.org/10.1029/GB001i001p00015>
- Carlson, A. E. (2008). Why there was not a younger dryas-like event during the penultimate deglaciation. *Quaternary Science Reviews*, 27(9), 882–887. <https://doi.org/10.1016/j.quascirev.2008.02.004>
- Chen, T., Robinson, L. F., Burke, A., Southon, J., Spooner, P., Morris, P. J., & Hong, C. N. (2015). Synchronous centennial abrupt events in the ocean and atmosphere during the last deglaciation. *Science*, 349(6255), 1537–1541. <https://doi.org/10.1126/science.aac6159>
- Cheng, H., Edwards, R. L., Broecker, W. S., Denton, G. H., Kong, X., Wang, Y., et al. (2009). Ice age terminations. *Science*, 326(5950), 248–252. <https://doi.org/10.1126/science.1177840>
- Cheng, H., Edwards, R. L., Sinha, A., Spötl, C., Yi, L., Chen, S., et al. (2016). The Asian monsoon over the past 640,000 years and ice age terminations. *Nature*, 534(7609), 640–646. <https://doi.org/10.1038/nature18591>
- Cheng, H., Zhang, H., Spötl, C., Baker, J., Sinha, A., Li, H., et al. (2020). Timing and structure of the Younger Dryas event and its underlying climate dynamics. *Proceedings of the National Academy of Sciences of the United States of America*, 117(38), 23408–23417. <https://doi.org/10.1073/pnas.2007869117>
- Clark, P. U., Dyke, A. S., Shakun, J. D., Carlson, A. E., Clark, J., Wohlfarth, B., et al. (2009). The last glacial maximum. *Science*, 325(5941), 710–714. <https://doi.org/10.1126/science.1172873>
- Clark, P. U., He, F., Gollledge, N. R., Mitrovica, J. X., Dutton, A., Hoffman, J. S., & Dendy, S. (2020). Oceanic forcing of penultimate deglacial and last interglacial sea-level rise. *Nature*, 577(7792), 660–664. <https://doi.org/10.1038/s41586-020-1931-7>
- Clark, P. U., Hostetler, S. W., Pisias, N. G., Schmittner, A., & Meissner, K. J. (2007). Mechanisms for an ~7-Kyr climate and sea-level oscillation during marine isotope stage 3. In A. Schmittner, J. C. H. Chiang, & S. R. Hemming (Eds.), *Ocean circulation: Mechanisms and impacts—Past and future changes of meridional overturning*. <https://doi.org/10.1029/173GM15>
- Curry, W. B., & Oppo, D. W. (2005). Glacial water mass geometry and the distribution of $\delta^{13}\text{C}$ of ΣCO_2 in the western Atlantic Ocean. *Paleoceanography*, 20(1), PA1017. <https://doi.org/10.1029/2004PA001021>
- Cutler, K. B., Edwards, R. L., Taylor, F. W., Cheng, H., Adkins, J., Gallup, C. D., et al. (2003). Rapid sea-level fall and deep-ocean temperature change since the last interglacial period. *Earth and Planetary Science Letters*, 206(3), 253–271. [https://doi.org/10.1016/S0012-821X\(02\)01107-X](https://doi.org/10.1016/S0012-821X(02)01107-X)
- Deaney, E. L., Barker, S., & van de Flierdt, T. (2017). Timing and nature of AMOC recovery across Termination 2 and magnitude of deglacial CO₂ change. *Nature Communications*, 8(1), 14595. <https://doi.org/10.1038/ncomms14595>
- Dokken, T. M., & Jansen, E. (1999). Rapid changes in the mechanism of ocean convection during the last glacial period. *Nature*, 401(6752), 458–461. <https://doi.org/10.1038/46753>
- Dyer, B., Austermann, J., D'Andrea, W. J., Creel, R. C., Sandstrom, M. R., Cashman, M., et al. (2021). Sea-level trends across The Bahamas constrain peak last interglacial ice melt. *Proceedings of the National Academy of Sciences of the United States of America*, 118(33), e2026839118. <https://doi.org/10.1073/pnas.2026839118>
- Eggleston, S., Schmitt, J., Bereiter, B., Schneider, R., & Fischer, H. (2016). Evolution of the stable carbon isotope composition of atmospheric CO₂ over the last glacial cycle. *Paleoceanography*, 31(3), 434–452. <https://doi.org/10.1002/2015PA002874>
- Ferrari, R., Jansen, M. F., Adkins, J. F., Burke, A., Stewart, A. L., & Thompson, A. F. (2014). Antarctic sea ice control on ocean circulation in present and glacial climates. *Proceedings of the National Academy of Sciences of the United States of America*, 111(24), 8753–8758. <https://doi.org/10.1073/pnas.1323922111>
- Garity, M., & Lund, D. C. (2023). NOAA/WDS paleoclimatology - Brazil Margin benthic foraminiferal B/Ca data from 50-150 ka [Dataset]. NOAA National Centers for Environmental Information. <https://doi.org/10.25921/2tjj-h043>
- Grant, K. M., Rohling, E. J., Bar-Matthews, M., Ayalon, A., Medina-Elizalde, M., Ramsey, C. B., et al. (2012). Rapid coupling between ice volume and polar temperature over the past 150,000 years. *Nature*, 491(7426), 744–747. <https://doi.org/10.1038/nature11593>
- Gu, S., Liu, Z., Oppo, D. W., Lynch-Stieglitz, J., Jahn, A., Zhang, J., et al. (2021). Remineralization dominating the $\delta^{13}\text{C}$ decrease in the mid-depth Atlantic during the last deglaciation. *Earth and Planetary Science Letters*, 571, 117106. <https://doi.org/10.1016/j.epsl.2021.117106>
- Hays, J. D., Imbrie, J., & Shackleton, N. J. (1976). Variations in the Earth's orbit: Pacemaker of the ice ages. *Science*, 194(4270), 1121–1132. <https://doi.org/10.1126/science.194.4270.1121>
- Hertzberg, J. E., Lund, D. C., Schmittner, A., & Skrivaneck, A. L. (2016). Evidence for a biological pump driver of atmospheric CO₂ rise during Heinrich Stadial 1. *Geophysical Research Letters*, 43(23), 12242–12251. <https://doi.org/10.1002/2016GL070723>
- Hodell, D. A., Minth, E. K., Curtis, J. H., McCave, I. N., Hall, I. R., Channell, J. E. T., & Xuan, C. (2009). Surface and deep-water hydrography on Gardar Drift (Iceland Basin) during the last interglacial period. *Earth and Planetary Science Letters*, 288(1), 10–19. <https://doi.org/10.1016/j.epsl.2009.08.040>
- Hoffman, J. L., & Lund, D. C. (2012). Refining the stable isotope budget for Antarctic Bottom Water: New foraminiferal data from the abyssal southwest Atlantic. *Paleoceanography*, 27(1), PA1213. <https://doi.org/10.1029/2011PA002216>

- Huybers, P., & Wunsch, C. (2005). Obliquity pacing of the late Pleistocene glacial terminations. *Nature*, 434(7032), 491–494. <https://doi.org/10.1038/nature03401>
- Imbrie, J., Berger, A., Boyle, E. A., Clemens, S. C., Duffy, A., Howard, W. R., et al. (1993). On the structure and origin of major glaciation cycles 2. The 100,000-year cycle. *Paleoceanography*, 8(6), 699–735. <https://doi.org/10.1029/93PA02751>
- Imbrie, J., Boyle, E. A., Clemens, S. C., Duffy, A., Howard, W. R., Kukla, G., et al. (1992). On the structure and origin of major glaciation cycles 1. Linear responses to Milankovitch forcing. *Paleoceanography*, 7(6), 701–738. <https://doi.org/10.1029/92PA02253>
- Kohfeld, K. E., & Chase, Z. (2017). Temporal evolution of mechanisms controlling ocean carbon uptake during the last glacial cycle. *Earth and Planetary Science Letters*, 472, 206–215. <https://doi.org/10.1016/j.epsl.2017.05.015>
- Koltermann, K. P., Gouretski, V. V., & Jancke, K. (2011). In M. Sparrow, P. Chapman, & J. Gould (Eds.), *Hydrographic Atlas of the World Ocean Circulation experiment (WOCE). Volume 3: Atlantic Ocean*. International WOCE Project Office. <https://doi.org/10.21976/C6RP4Z>
- Lacerra, M., Lund, D., Yu, J., & Schmittner, A. (2017). Carbon storage in the mid-depth Atlantic during millennial-scale climate events: Mid-depth Atlantic carbon storage. *Paleoceanography*, 32(8), 780–795. <https://doi.org/10.1002/2016PA003081>
- Lacerra, M., Lund, D. C., Gebbie, G., Oppo, D. W., Yu, J., Schmittner, A., & Umling, N. E. (2019). Less remineralized carbon in the intermediate-depth South Atlantic during Heinrich Stadial 1. *Paleoceanography and Paleoclimatology*, 34(7), 1218–1233. <https://doi.org/10.1029/2018PA003537>
- Laskar, J., Robutel, P., Joutel, F., Gastineau, M., Correia, A. C. M., & Levrard, B. (2004). A long-term numerical solution for the insolation quantities of the Earth. *Astronomy and Astrophysics*, 428(1), 261–285. <https://doi.org/10.1051/0004-6361:20041335>
- Lippold, J. Ö., Grützner, J., Winter, D., Lahaye, Y., Mangini, A., & Christl, M. (2009). Does sedimentary $^{231}\text{Pa}/^{230}\text{Th}$ from the Bermuda rise monitor past Atlantic meridional overturning circulation? *Geophysical Research Letters*, 36(12), L12601. <https://doi.org/10.1029/2009GL038068>
- Lisiecki, L. E. (2014). Atlantic overturning responses to obliquity and precession over the last 3 Myr. *Paleoceanography*, 29(2), 71–86. <https://doi.org/10.1002/2013PA002505>
- Lisiecki, L. E., & Raymo, M. E. (2005). A Pliocene-Pleistocene stack of 57 globally distributed benthic $\delta^{18}\text{O}$ records. *Paleoceanography*, 20(1), PA1003. <https://doi.org/10.1029/2004PA001071>
- Lisiecki, L. E., Raymo, M. E., & Curry, W. B. (2008). Atlantic overturning responses to Late Pleistocene climate forcings. *Nature*, 456(7218), 85–88. <https://doi.org/10.1038/nature07425>
- Lisiecki, L. E., & Stern, J. V. (2016). Regional and global benthic $\delta^{18}\text{O}$ stacks for the last glacial cycle. *Paleoceanography*, 31(10), 1368–1394. <https://doi.org/10.1002/2016PA003002>
- Lourantou, A., Lavrič, J. V., Köhler, P., Barnola, J., Paillard, D., Michel, E., et al. (2010). Constraint of the CO_2 rise by new atmospheric carbon isotopic measurements during the last deglaciation. *Global Biogeochemical Cycles*, 24(2). <https://doi.org/10.1029/2009GB003545>
- Lund, D., Hertzberg, J., & Lacerra, M. (2019). Carbon isotope minima in the South Atlantic during the last deglaciation: Evaluating the influence of air-sea gas exchange. *Environmental Research Letters*, 14(5), 055004. <https://doi.org/10.1088/1748-9326/ab126f>
- Lund, D. C., Tessin, A. C., Hoffman, J. L., & Schmittner, A. (2015). Southwest Atlantic water mass evolution during the last deglaciation. *Paleoceanography*, 30(5), 477–494. <https://doi.org/10.1002/2014PA002657>
- Lynch-Stieglitz, J., Stocker, T. F., Broecker, W. S., & Fairbanks, R. G. (1995). The influence of air-sea exchange on the isotopic composition of oceanic carbon: Observations and modeling. *Global Biogeochemical Cycles*, 9(4), 653–665. <https://doi.org/10.1029/95GB02574>
- Lynch-Stieglitz, J., Valley, S. G., & Schmidt, M. W. (2019). Temperature-dependent ocean-atmosphere equilibration of carbon isotopes in surface and intermediate waters over the deglaciation. *Earth and Planetary Science Letters*, 506, 466–475. <https://doi.org/10.1016/j.epsl.2018.11.024>
- MacFarling Meure, C., Etheridge, D., Trudinger, C., Steele, P., Langenfelds, R., van Ommen, T., et al. (2006). Law Dome CO_2 , CH_4 and N_2O ice core records extended to 2000 years BP. *Geophysical Research Letters*, 33(14), L14810. <https://doi.org/10.1029/2006GL026152>
- Marcott, S. A., Bauska, T. K., Buizert, C., Steig, E. J., Rosen, J. L., Cuffey, K. M., et al. (2014). Centennial-scale changes in the global carbon cycle during the last deglaciation. *Nature*, 514(7524), 616–619. <https://doi.org/10.1038/nature13799>
- Marcott, S. A., Clark, P. U., Padman, L., Klinkhammer, G. P., Springer, S. R., Liu, Z., et al. (2011). Ice-shelf collapse from subsurface warming as a trigger for Heinrich events. *Proceedings of the National Academy of Sciences of the United States of America*, 108(33), 13415–13419. <https://doi.org/10.1073/pnas.1104772108>
- Maslin, M. A., & Swann, G. E. A. (2006). Isotopes in marine sediments. In M. J. Leng (Ed.), *Isotopes in palaeoenvironmental research* (pp. 227–290). Springer Netherlands. https://doi.org/10.1007/1-4020-2504-1_06
- McManus, J. F., Francois, R., Gherardi, J., Keigwin, L. D., & Brown-Leger, S. (2004). Collapse and rapid resumption of Atlantic meridional circulation linked to deglacial climate changes. *Nature*, 428(6985), 834–837. <https://doi.org/10.1038/nature02494>
- McManus, J. F., Oppo, D. W., & Cullen, J. L. (1999). A 0.5-million-year record of millennial-scale climate variability in the North Atlantic. *Science*, 283(5404), 971–975. <https://doi.org/10.1126/science.283.5404.971>
- Milliman, J. D. (1993). Production and accumulation of calcium carbonate in the ocean: Budget of a nonsteady state. *Global Biogeochemical Cycles*, 7(4), 927–957. <https://doi.org/10.1029/93GB02524>
- Monnin, E., Indermühle, A., Dällenbach, A., Flückiger, J., Stauffer, B., Stocker, T. F., et al. (2001). Atmospheric CO_2 concentrations over the last glacial termination. *Science*, 291(5501), 112–114. <https://doi.org/10.1126/science.291.5501.112>
- Monnin, E., Steig, E. J., Siegenthaler, U., Kawamura, K., Schwander, J., Stauffer, B., et al. (2004). Evidence for substantial accumulation rate variability in Antarctica during the Holocene, through synchronization of CO_2 in the Taylor Dome, Dome C and DML ice cores. *Earth and Planetary Science Letters*, 224(1), 45–54. <https://doi.org/10.1016/j.epsl.2004.05.007>
- Obase, T., Abe-Ouchi, A., & Saito, F. (2021). Abrupt climate changes in the last two deglaciations simulated with different Northern ice sheet discharge and insolation. *Scientific Reports*, 11(1), 22359. <https://doi.org/10.1038/s41598-021-01651-2>
- Oliver, K. I. C., Hoogakker, B. A. A., Crowhurst, S., Henderson, G. M., Rickaby, R. E. M., Edwards, N. R., & Elderfield, H. (2010). A synthesis of marine sediment core $\delta^{13}\text{C}$ data over the last 150 000 years. *Climate of the Past*, 6(5), 645–673. <https://doi.org/10.5194/cp-6-645-2010>
- Oppo, D. W., Curry, W. B., & McManus, J. F. (2015). What do benthic $\delta^{13}\text{C}$ and $\delta^{18}\text{O}$ data tell us about Atlantic circulation during Heinrich Stadial 1? *Paleoceanography*, 30(4), 353–368. <https://doi.org/10.1002/2014PA002667>
- Oppo, D. W., Horowitz, M., & Lehman, S. J. (1997). Marine core evidence for reduced deep water production during Termination II followed by a relatively stable substage 5e (Eemian). *Paleoceanography*, 12(1), 51–63. <https://doi.org/10.1029/96PA03133>
- Osman, M. B., Tierney, J. E., Zhu, J., Tardif, R., Hakim, G. J., King, J., & Poulsen, C. J. (2021). Globally resolved surface temperatures since the last glacial maximum. *Nature*, 599(7884), 239–244. <https://doi.org/10.1038/s41586-021-03984-4>
- Ostermann, D. R., & Curry, W. B. (2000). Calibration of stable isotopic data: An enriched $\delta^{18}\text{O}$ standard used for source gas mixing detection and correction. *Paleoceanography*, 15(3), 353–360. <https://doi.org/10.1029/1999PA000411>
- Parrenin, F., & Paillard, D. (2003). Amplitude and phase of glacial cycles from a conceptual model. *Earth and Planetary Science Letters*, 214(1), 243–250. [https://doi.org/10.1016/S0012-821X\(03\)00363-7](https://doi.org/10.1016/S0012-821X(03)00363-7)

- Pierrot, D. E., Lewis, & Wallace (2006). *MS excel program developed for CO₂ system calculations*. ORNL/CDIAC-105a. Carbon Dioxide Information Analysis Center, Oak Ridge National Laboratory, U.S. Department of Energy. https://doi.org/10.3334/CDIAC/otg.CO2SYS_XLS_CDIAC105a
- Piotrowski, A. M., Goldstein, S. L., Hemming, S. R., & Fairbanks, R. G. (2005). Temporal relationships of carbon cycling and ocean circulation at glacial boundaries. *Science*, 307(5717), 1933–1938. <https://doi.org/10.1126/science.1104883>
- Praetorius, S. K., McManus, J. F., Oppo, D. W., & Curry, W. B. (2008). Episodic reductions in bottom-water currents since the last ice age. *Nature Geoscience*, 1(7), 449–452. <https://doi.org/10.1038/ngeo227>
- Rasmussen, S. O., Andersen, K. K., Svensson, A. M., Steffensen, J. P., Vinther, B. M., Clausen, H. B., et al. (2006). A new Greenland ice core chronology for the last glacial termination. *Journal of Geophysical Research*, 111(D6), D06102. <https://doi.org/10.1029/2005JD006079>
- Rickaby, R. E. M., & Elderfield, H. (2005). Evidence from the high-latitude North Atlantic for variations in Antarctic Intermediate water flow during the last deglaciation. *Geochemistry, Geophysics, Geosystems*, 6(5), Q05001. <https://doi.org/10.1029/2004GC000858>
- Rohling, E. J., Grant, K., Bolshaw, M., Roberts, A. P., Siddall, M., Hemleben, C., & Kucera, M. (2009). Antarctic temperature and global sea level closely coupled over the past five glacial cycles. *Nature Geoscience*, 2(7), 500–504. <https://doi.org/10.1038/ngeo557>
- Rubino, M., Etheridge, D. M., Trudinger, C. M., Allison, C. E., Battle, M. O., Langenfelds, R. L., et al. (2013). A revised 1000 year atmospheric $\delta^{13}\text{C}$ -CO₂ record from Law Dome and South Pole, Antarctica. *Journal of Geophysical Research: Atmospheres*, 118(15), 8482–8499. <https://doi.org/10.1002/jgrd.50668>
- Schlitzer, R. (2015). Ocean data view. [Available at odv.awi.de].
- Schmittner, A. (2005). Decline of the marine ecosystem caused by a reduction in the Atlantic overturning circulation. *Nature*, 434(7033), 628–633. <https://doi.org/10.1038/nature03476>
- Schmittner, A., & Lund, D. C. (2015). Early deglacial Atlantic overturning decline and its role in atmospheric CO₂ rise inferred from carbon isotopes ($\delta^{13}\text{C}$). *Climate of the Past*, 11(2), 135–152. <https://doi.org/10.5194/cp-11-135-2015>
- Schneider, R., Schmitt, J., Kehler, P., Joos, F., & Fischer, H. (2013). A reconstruction of atmospheric carbon dioxide and its stable carbon isotopic composition from the penultimate glacial maximum to the last glacial inception. *Climate of the Past*, 9(6), 2507–2523. <https://doi.org/10.5194/cp-9-2507-2013>
- Shackleton, S., Menking, J. A., Brook, E., Buizert, C., Dyonisius, M. N., Petrenko, V. V., et al. (2021). Evolution of mean ocean temperature in marine isotope stage 4. *Climate of the Past*, 17(5), 2273–2289. <https://doi.org/10.5194/cp-17-2273-2021>
- Shaffer, G., Olsen, S. M., & Bjerrum, C. J. (2004). Ocean subsurface warming as a mechanism for coupling Dansgaard-Oeschger climate cycles and ice-rafting events. *Geophysical Research Letters*, 31(24), L24202. <https://doi.org/10.1029/2004GL020968>
- Shakun, J. D., Clark, P. U., He, F., Marcott, S. A., Mix, A. C., Liu, Z., et al. (2012). Global warming preceded by increasing carbon dioxide concentrations during the last deglaciation. *Nature*, 484(7392), 49–54. <https://doi.org/10.1038/nature10915>
- Shakun, J. D., Lea, D. W., Lisiecki, L. E., & Raymo, M. E. (2015). An 800-kyr record of global surface ocean $\delta^{18}\text{O}$ and implications for ice volume-temperature coupling. *Earth and Planetary Science Letters*, 426, 58–68. <https://doi.org/10.1016/j.epsl.2015.05.042>
- Shub, A., Lund, D. C., Oppo, D. W., & Garity, M. (2023). NOAA/WDS paleoclimatology—Brazil Margin stable isotope data for the last glacial cycle [Dataset]. NOAA National Centers for Environmental Information. <https://doi.org/10.25921/n443-0561>
- Shub, A. B., Lund, D. C., Oppo, D. W., & Garity, M. L. (2024). Brazil Margin stable isotope profiles for the last glacial cycle: Implications for watermass geometry and oceanic carbon storage. *Paleoceanography and Paleoclimatology*. <https://doi.org/10.1029/2023PA004635>
- Sigman, D. M., & Boyle, E. A. (2000). Glacial/interglacial variations in atmospheric carbon dioxide. *Nature*, 407(6806), 859–869. <https://doi.org/10.1038/35038000>
- Snyder, C. (2016). Evolution of global temperature over the past two million years. *Nature*, 538(7624), 226–228. <https://doi.org/10.1038/nature19798>
- Spratt, R. M., & Lisiecki, L. E. (2016). A Late Pleistocene sea level stack. *Climate of the Past*, 12(4), 1079–1092. <https://doi.org/10.5194/cp-12-1079-2016>
- Tessin, A. C., & Lund, D. C. (2013). Isotopically depleted carbon in the mid-depth South Atlantic during the last deglaciation. *Paleoceanography and Paleoclimatology*, 28(2), 296–306. <https://doi.org/10.1002/palo.20026>
- Thornalley, D. J. R., Elderfield, H., & McCave, I. N. (2010). Intermediate and deep water paleoceanography of the northern North Atlantic over the past 21,000 years. *Paleoceanography*, 25(1), PA1211. <https://doi.org/10.1029/2009PA001833>
- Tierney, J. E., Zhu, J., King, J., Malevich, S., Hakim, G., & Poulsen, C. (2020). Glacial cooling and climate sensitivity revisited. *Nature*, 584(7822), 569–573. <https://doi.org/10.1038/s41586-020-2617-x>
- Toggweiler, J. R. (1999). Variation of atmospheric CO₂ by ventilation of the ocean's deepest water. *Paleoceanography*, 14(5), 571–588. <https://doi.org/10.1029/1999PA000033>
- Tzedakis, P. C., Crucifix, M., Mitsui, T., & Wolff, E. W. (2017). A simple rule to determine which insolation cycles lead to interglacials. *Nature*, 542(7642), 427–432. <https://doi.org/10.1038/nature21364>
- Venz, K. A., Hodell, D. A., Stanton, C., & Warnke, D. A. (1999). A 1.0 Myr record of Glacial North Atlantic intermediate water variability from ODP site 982 in the Northeast Atlantic. *Paleoceanography*, 14(1), 42–52. <https://doi.org/10.1029/1998PA000013>
- Waelbroeck, C., Labeyrie, L., Michel, E., Duplessy, J. C., McManus, J. F., Lambeck, K., et al. (2002). Sea-level and deep water temperature changes derived from benthic foraminifera isotopic records. *Quaternary Science Reviews*, 21(1), 295–305. [https://doi.org/10.1016/S0277-3791\(01\)00101-9](https://doi.org/10.1016/S0277-3791(01)00101-9)
- Wilson, D. J., Piotrowski, A. M., Galy, A., & Banakar, V. K. (2015). Interhemispheric controls on deep ocean circulation and carbon chemistry during the last two glacial cycles. *Paleoceanography*, 30(6), 621–641. <https://doi.org/10.1002/2014PA002707>
- Xie, R. C., Marcantonio, F., & Schmidt, M. W. (2012). Deglacial variability of Antarctic Intermediate Water penetration into the North Atlantic from authigenic neodymium isotope ratios. *Paleoceanography*, 27(3). <https://doi.org/10.1029/2012PA002337>
- Yu, J., Anderson, R., & Rohling, E. (2014). Deep Ocean carbonate chemistry and glacial-interglacial atmospheric CO₂ change. *Oceanography*, 27(1), 16–25. <https://doi.org/10.5670/oceanog.2014.04>
- Yu, J., Anderson, R. F., Jin, Z., Rae, J. W. B., Opdyke, B. N., & Eggins, S. M. (2013). Responses of the deep ocean carbonate system to carbon reorganization during the Last Glacial–interglacial cycle. *Quaternary Science Reviews*, 76, 39–52. <https://doi.org/10.1016/j.quascirev.2013.06.020>
- Yu, J., Broecker, W. S., Elderfield, H., Jin, Z., McManus, J., & Zhang, F. (2010). Loss of carbon from the deep sea since the last glacial maximum. *Science*, 330(6007), 1084–1087. <https://doi.org/10.1126/science.1193221>
- Yu, J., & Elderfield, H. (2007). Benthic foraminiferal B/Ca ratios reflect deep water carbonate saturation state. *Earth and Planetary Science Letters*, 258(1), 73–86. <https://doi.org/10.1016/j.epsl.2007.03.025>
- Yu, J., Meniel, L., Jin, Z. D., Thornalley, D. J. R., Barker, S., Marino, G., et al. (2016). Sequestration of carbon in the deep Atlantic during the last glaciation. *Nature Geoscience*, 9(4), 319–324. <https://doi.org/10.1038/ngeo2657>